OPTICAL MODELING AND RESIST METROLOGY FOR DEEP-UV PHOTOLITHOGRAPHY

A Thesis

by

CHAO LIU

Submitted to the Office of Graduate Studies of
Texas A&M University
in partial fulfillment of the requirements for the degree of

MASTER OF SCIENCE

August 2005

Major Subject: Electrical Engineering

OPTICAL MODELING AND RESIST METROLOGY FOR DEEP-UV PHOTOLITHOGRAPHY

A Thesis

by

CHAO LIU

Submitted to the Office of Graduate Studies of
Texas A&M University
in partial fulfillment of the requirements for the degree of

MASTER OF SCIENCE

Approved by:

Co-Chairs of Committee,	Mosong Cheng
	Ohannes Eknoyan
Committee Members,	Chin B. Su
	Krzysztof A. Michalski
	Yue Kuo
Head of Department,	Chanan Singh

August 2005

Major Subject: Electrical Engineering

ABSTRACT

Optical Modeling and Resist Metrology for Deep-UV Photolithography.

(August 2005)

Chao Liu, B.S., Tsinghua University

Co-Chairs of Advisory Committee: Dr. Mosong Cheng
Dr. Ohannes Eknoyan

This thesis first presents a novel and highly accurate methodology for investigating the kinetics of photoacid diffusion and catalyzed-deprotection of positive-tone chemically amplified resists during post exposure bake (PEB) by in-situ monitoring the change of resist and capacitance (RC) of resist film during PEB. Deprotection converts the protecting group to volatile group, which changes the dielectric constant of resist. So the deprotection rate can be extracted from the change of capacitance. The photoacid diffusivity is extracted from the resistance change because diffusivity determines the rate of change of the acid distribution. Furthermore, by comparing the R and C curves, the dependence of acid diffusivity on reaction state can be extracted. The kinetics of non-Fickean acid transportation, deprotection, free volume generation and absorption/escaping, and resist shrinkage is analyzed and a comprehensive model is proposed that includes these chemical/physical mechanisms.

Then in this thesis a novel lithographic technique, liquid immersion contact lithography (LICL) is proposed and the simulations are performed to illustrate its main

features and advantages. Significant depth-of-field (DOF) enhancement can be achieved for large pitch gratings with deep-UV light (λ=248nm) illumination with both TM and TE polarizations by liquid immersion. Better than 100nm DOF can be achieved by when printing 70nm apertures. The simulation results show that it is very promising to apply this technique in scanning near field optical microscopy.

Finally, a rigorous, full vector imaging model of non-ideal mask is developed and the simulation of the imaging of such a mask with 2D roughness is performed. Line edge roughness (LER) has been a major issue limiting the performance of sub-100nm photolithography. A lot of factors contribute to LER, including mask roughness, lens imperfection, resist chemistry, process variation, etc. To evaluate the effect of mask roughness on LER, a rigorous full vector model has been developed by the author. We calculate the electromagnetic (EM) field immediately after a rough mask by using TEMPEST and simulate the projected wafer image with SPLAT. The EM field and wafer image deviate from those from an ideal mask. LER is finally calculated based on the projected image.

DEDICATION

To My Parents

ACKNOWLEDGMENTS

I would like to express my gratitude to all those who helped me complete this thesis. I want to thank Dr. M. Cheng for serving as my committee co-chair and for his stimulating suggestions and encouragement during these past years. I would also like to thank Dr. O. Eknoyan for providing advice and help in addition to being my co-chair. Thanks to Dr. C. B. Su, Dr. K. A. Michalski and Dr. Y. Kuo for also serving on my committee and helping on my thesis.

I am grateful to Mr. R. A. Atkins, our lab manager, for his technical training and support in my research. Without his help, this thesis could never have been finished.

And needless to say, I am grateful to all of my friends and colleagues, Y. Ping, N. Jing, M. Wang, S. Seo and Y. Shin, for their friendship and help.

I would like to give my special thanks to my wife for being with me every single moment. And finally, I thank my parents for their love and encouragement.

TABLE OF CONTENTS

Page

ABSTRACT……..... iii

DEDICATION……..……..... v

ACKNOWLEDGMENTS…….……..…….. vi

TABLE OF CONTENTS……..……..... vii

LIST OF FIGURES……..…….. ix

LIST OF TABLES…….……..……. xii

CHAPTER

I INTRODUCTION……..…… 1

II CHEMICALLY AMPLIFIED PHOTORESIST CHARACTERIZATION … 4

A. Background……..…… 4
B. Introduction…….....…… 13
C. Experiment Setup…….……...…….…… 16
D. Qualitative Analysis and PEB Model…… 18
E. Experimental Results and Parameter Extraction……. 23
F. Conclusion……..…….…….. 30

III IMPROVING RESOLUTION AND DEPTH OF FIELD IN NEAR FIELD OPTICAL PATTERNING VIA LIQUID IMMERSION IMAGING……. 32

A. Introduction..…….…… 32
1. Interferometric lithography……..…….. 33
2. PSMs in contact printing……...……...……...… 34
3. Light-coupling mask……..…… 36
4. Step and flash imprint lithography….……..…… 38
B. Simulation Methods and Models……..……. 40

TABLE OF CONTENTS (Continued)

CHAPTER

Page

C. Results and Discussions…… 42
1. Dense line…… 42
(1) Field enhancement…….. 44
(2) DOF of dense lines…… 45
2. Isolated aperture.……...…….. 47
(1) Improvement of DOF……..…… 48
(2) Trend of DOF…….…… 49
(3) Exception…….…… 50
D. Conclusion……..... 51

IV RIGOROUS ELECTROMAGNETIC ANALYSIS OF MASK ROUGHNESS EFFECTS IN VERY HIGH NA LITHOGRAPHY…..…..... 53

A. Overview of Major Types of Masks.…….……..…… 53
1. Binary mask…….……...……. 53
2. Attenuated phase-shift mask (AttPSM)……...…… 54
3. Chromeless phase lithography technology mask……...….. 55
4. Alternating phase-shift mask (AltPSM)……..……. 56
B. Introduction……. 57
C. Simulation Methods and Models……..…….. 58
D. Results and Discussions…….. 60
1. Grating…….……..…….. 60
(1) Attenuated phase-shift mask…….. 60
(2) Alternating phase-shift mask……. 63
2. Contact…….....…….…… 65
(1) Attenuated phase-shift mask……. 65
(2) Cr binary mask…….……. 66
E. Conclusion……..…… 67

V CONCLUSION……..……..……. 69

REFERENCES…….…… 71

VITA…….. 75

LIST OF FIGURES

FIGURE		Page
1	Intel lithography roadmap……..…….....	2
2	Imaging chemistry of a typical positive-tone chemically amplified resist.…	5
3	General mechanism for acid-catalyzed hydrolysis of a ketal…….	7
4	Experiment setup……..……..…….……	17
5	RC measurement, exposure dose 75mJ/cm^2, PEB 130°C…….	19
6	Normalized resist thickness vs. PEB time……...	20
7	Capacitance and resistance variations during PEB (a) Capacitance (b) Resistance.……...……...……..…..	25
8	Extracting reaction rate constant k_1 from ln(C_1-C) vs. t…….....	26
9	Resistance variation in 130°C PEB……..……	26
10	Simulated and experimental RC curves, (a) R, (b) C at PEB 130ºC.....….	29
11	Normalized photoacid concentration, dose 75mJ/cm^2…….…….....	30
12	Geometry of the optical system……..……..…	35
13	Variation of the pattern intensity as a function of the shift of the phase..…	36
14	Schematic of light passing through a structured polymer in contact with a resist…….……...…….	37
15	Step and flash lithography process sequence...…….	39

LIST OF FIGURES (Continued)

FIGURE Page

16 Geometry of the grating system……..……..…….... 41

17 Light intensity profile for 140nm grating immersed in liquid with TE and TM polarized light of 248nm illumination (a) TM polarized (b) TE polarized……...…… 43

18 Intensity line plots of same exposure condition as Figure 17.…… 44

19 The ILS and the contrast of the diffracted near field versus the distance from the exit plane of the grating……...…..…… 47

20 DOF vs. pitch p for simulated gratings plots for TM and TE polarized illumination…….…….. 48

21 ILS vs. distance from the exit plane of the grating for 600nm pitch grating with illumination of TE polarized light…….…….. 51

22 Light intensity in resist after an attenuated phase-shift mask……..... 55

23 Light intensity in resist after a chromeless phase lithography mask…..…….. 56

24 Light intensity in resist after an alternating phase-shift mask……..…... 57

25 Overview of the aerial image simulation flow.…….…….... 59

26 Masks with and without roughness and their corresponding light intensity distribution immediately after the masks under 193nm wavelength TE illumination…….…….. 60

27 Image light intensity distribution and cross-section after ×4 lens for two 1:1, 520nm pitch grating attenuated PSMs with 15% transmission in the dark region, illuminated by 193nm wavelength and TE polarization……. 61

LIST OF FIGURES (Continued)

FIGURE Page

28 Image contrast vs. LER on the mask under TE and TM polarized illumination for attPSM……...……..…… 63

29 The image light intensity distribution and cross-section after ×4 lens for a 1:1, 520nm pitch alternating PSM…….…….……. 64

30 Image contrast vs. LER on the mask under TE and TM polarized illumination for altPSM…….…….…….…… 65

31 Phase distribution of the light field immediately after the attenuated PSM for a contact under illumination of a circular polarized incident field…… 66

32 Average contact diameter vs. LER on the mask for Cr mask.....……. 67

LIST OF TABLES

TABLE Page

1 Typical pK_a values for function groups of importance in chemically amplified resist chemistry……..……..……..… 8

2 Typical values for diffusion coefficient D…… 13

CHAPTER I

INTRODUCTION

Ever since Gorden Moore made his famous observation in 1965 that the number of transistors in the integrated circuit will double every couple of years, which is the so-called Moore's Law, this trend has been maintained and still holds true today.

The speed and performance of the integrated circuit chips, their associated systems, are mainly determined by the minimum printable size during fabrication, which is basically determined by photolithography process. Because of the importance of lithography, semiconductor industry developed a strategic and tactical roadmap for the future direction of lithography technology. The roadmap is the plan for the lithography technology that will be used to pattern the smallest features on each new generation of integrated circuits. Figure 1 shows the Intel lithography roadmap,[1] which is aligned with the whole semiconductor industry. Currently, 193nm lithography is used for the 90nm generation and will be used in 65nm generation.

A traditional photolithography process can be divided into two steps. The first step is an optical process, which transfers the information in a patterned mask to the photoresist (a light-sensitive material) on the wafer by forming a certain electrical field inside the

---

This thesis follows the style and format of Journal of Vacuum Science & Technology B.

photoresist. The second step is a chemical process, during which the formation of the photoresist is changed according to the distribution of the electrical field to form the desired pattern. Sometimes this process happens at the same time when the wafer is illuminated, and sometimes it needs an extra thermal process, which is called post exposure bake (PEB) to finish this chemical process. At the end of the lithography process, the photoresist is used to create a useful structure in the device that is being built. For example, trenches can be etched into an insulator, or a uniform coating of metal can be etched to leave a network of electrical wiring on the surface of a semiconductor chip. The purpose of the photoresist is to serve as a hard mask during the subsequent etching process.

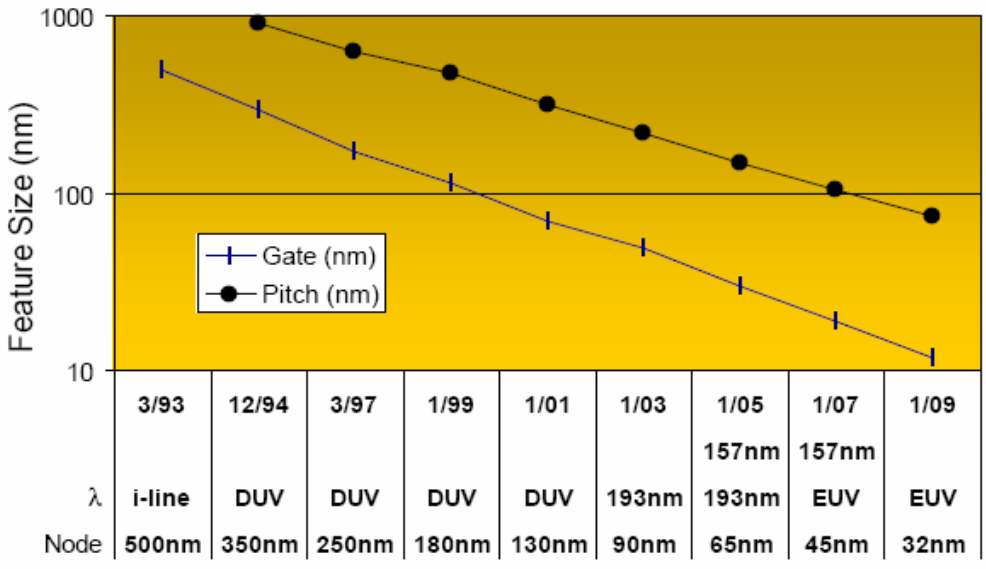

Fig. 1. Intel lithography roadmap.

An accurate understanding of what really happens during photolithography is highly needed to optimize this process, which needs both photoresist characterization and optical modeling.

The primary purpose of my research includes developing an accurate method for resist metrology, investigating a new resolution enhancement technique and analyzing the mask roughness impact on the printed line-edge roughness, for deep-UV photolithography.

The detailed description of resist metrology technique is provided in Chapter II. A novel resolution enhancement technique as well as its performance analysis is presented in Chapter III. The impact of mask roughness on the printed line-edge roughness in high NA (numerical aperture) lithography is analyzed in Chapter IV. Finally, conclusions are summarized in Chapter V.

CHAPTER II

CHEMICALLY AMPLIFIED PHOTORESIST CHARACTERIZATION

In this chapter, a novel and highly accurate methodology is presented for investigating the kinetics of photoacid diffusion and catalyzed-deprotection of positive-tone chemically amplified resists during post exposure bake (PEB) by in-situ monitoring the change of resistance and capacitance (RC) of resist film during PEB. The effects of free volume, polymer relaxation and deprotection-induced polarity change on acid diffusion are also identified.

A. Background

Chemically amplified resist (CAR) systems are based on the acid catalyzed deprotection of functioning groups in a polymer matrix that protect the polymer backbone from dissolution. Image formation in a positive-tone chemically amplified resist requires conversion of such a polymer matrix from insoluble to soluble. Though different resist for a specific application has different details of how this conversion is achieved, the imaging chemistry of all positive-tone chemically amplified resists is based on the similar sequence of transformations illustrated in Fig. 2.[2] First the photosensitive functioning group works as a photoacid generator by forming a proton-anion pair as one of its reaction products at the exposure of light or charged particle. Then this proton

causes a fragmentation or deprotection reaction of an ester, and generates a carboxylic acid. The ester fragmentation also forms a carbocation, an unstable species which ultimately deactivates by transferring the proton to another ester group in the polymer. Consequently, the deprotection occurs in this second ester group, and the proton is transferred to the third ester group as before, initiating a third cycle. This process of reaction and regeneration enables each proton to affect the deprotection of many ester groups in the polymer matrix, achieving an overall enhancement (or chemical amplification) of the initial latent image. In an aqueous alkaline developer, the carboxylic acid groups formed during deprotection will be ionized, making the polymer soluble in the aqueous solution.

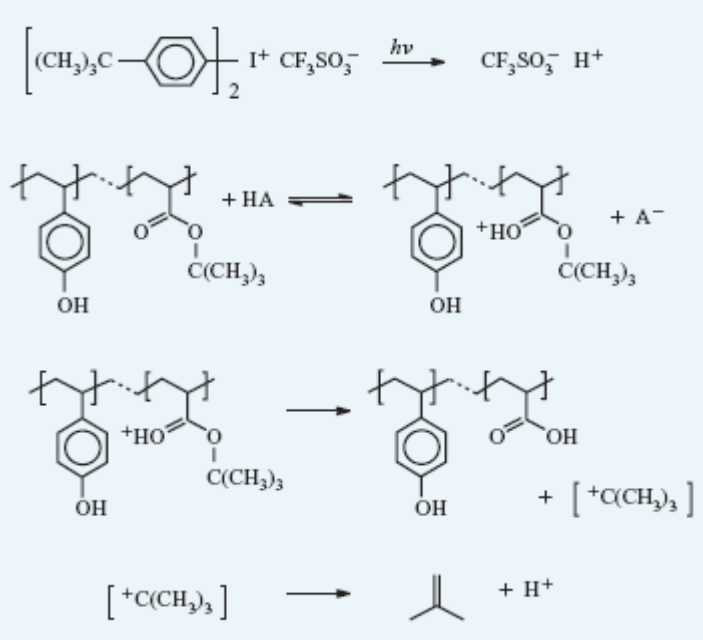

Fig. 2. Imaging chemistry of a typical positive-tone chemically amplified resist.

The proton formed in the reaction in Fig. 3 is regarded as an acid. Virtually all positive-tone chemically amplified resist systems uses an acid as a catalyst in their imaging formation. A catalyst is a substance that participates in a particular chemical reaction and thereby increases the reaction rate and remains unchanged at the end of the reaction. Acid-catalyzed reactions can be described by a mechanism that includes the two generic reaction steps:

$HA+S \rightleftharpoons HS^{+}+A^{-}$ (Step 1)

$HS^{+} \rightarrow \text{Products}$ (Step 2)

Step 1 is a reversible reaction in which the reactant S and acid catalyst HA combine to form a transient intermediate HS^{+}. This intermediate is unstable and can undergo some chemical reaction to produce a new product species (represented by Step 2), or Step 1 can reverse, regenerating HA and S. Chemists classify acid-catalyzed reactions as involving either general acid catalysis (when Step 2, the product-forming step, is fast compared to Step 1) or specific acid catalysis (when Step 2 is slow compared to Step 1), depending on the relative rates of the two steps.

Two types of acid-labile protecting groups have been most frequently used in positive-tone chemically amplified resist design: reactive esters, whose deprotection chemistry is shown in Fig. 2, and ketals, whose acid-catalyzed hydrolysis is depicted in Fig. 3.[2]

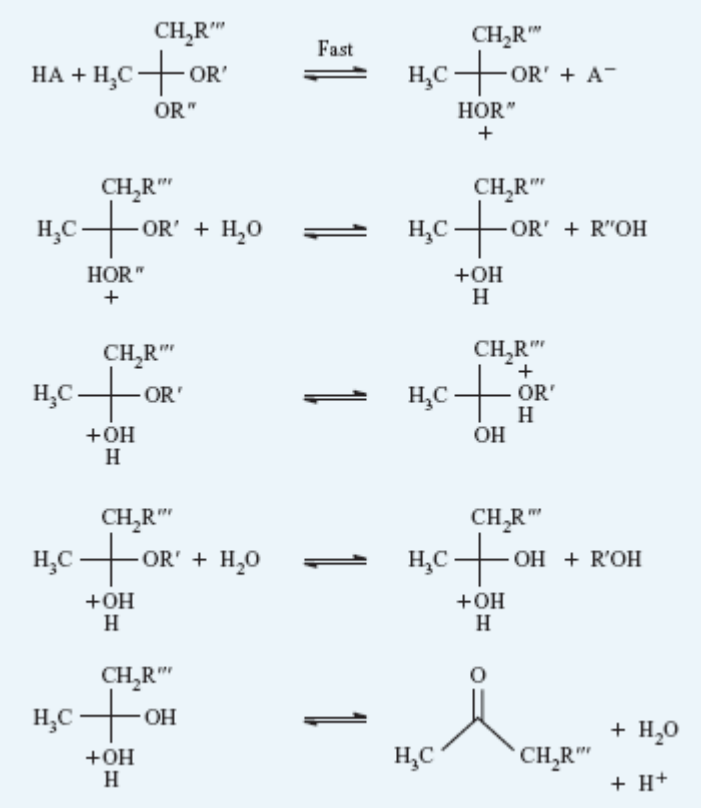

Fig. 3. General mechanism for acid-catalyzed hydrolysis of a ketal.

These reactions are considered to happen by specific acid catalysis in solution. So the overall deprotection rate is determined by the rate of Step 2 and is proportional to the concentration of the intermediate HS^{+}, which is generated by equilibration of that step. Its concentration in turn is determined by both the acidity of the acid HA (its ability to give up a proton), and the basicity of the substrate S (its ability to accept a proton). These properties can be quantified using the pK_a scale used to characterize acidity and basicity. The pK_a value for the dissociation of an acid HA is defined as the negative base-10 logarithm of the acid dissociation constant. Table 1 lists pK_a values for a

selection of acidic functional groups found in chemically amplified resist compositions.[2] The range of acid strengths of interest spans almost 20 orders of magnitude.

Table 1. Typical pK_a values for functional groups of importance in chemically amplified resist chemistry.

Functional group	Acidic form	Basic form	pK_a
Triflic acid	CF_3SO_3H	$CF_3SO_3^-$	(>-12)
Aromatic ester	$ArCOORH^+$	ArCOOR	-7.4
Aryl sulfonic	$ArSO_3H$	$ArSO_3^-$	-6.5
Aliphatic ester	$RCOORH^+$	RCOOR	-6.5
Phenol	$ArOH_2^+$	ArOH	-6.4
Ether	$ArORH^+$	ArOR	-6
Carboxylic	$RCOOH_2^+$	RCOOH	-6
Ether	$RORH^+$	ROR	-3.5
Amide	$RCONR_2H^+$	$RCONR_2$	-0.75
Alkyl sulfonic	RSO_3H	RSO_3^-	0
Aryl amine	$ArNHR_2H^+$	$ArNHR_2$	4
Carboxylic acid	RCOOH	$RCOO^-$	5
Secondary amine	$R_2NH_2^+$	R_2NH	11

A catalyst accelerates the rate of a reaction but is not consumed during the reaction. The rate is increased because with the existence of the catalyst, it provides an alternate route to the products with lower-energy requirements to bypass the previous higher one. The rate R of a reaction is written as

$$R = k_{obs} \prod C_n \tag{1}$$

where k_{obs} is the observed rate constant, and C_n represent the concentrations of the reactants. The relationship between the rate of the reaction and its energy requirements is defined in terms of the Arrhenius equation:

$$k_{obs} = A \exp(-E_a / RT) \tag{2}$$

where A is the pre-exponential factor, R is the gas constant, T is absolute temperature, and E_a is the activation energy which expresses the temperature dependence of the rate constant. In fact, the Arrhenius parameters A and E_a are fitting parameters for a set of data: they may or may not provide information on individual reaction events; the kineticist must decide whether or not the rate constant applies to only a single elementary reaction step or a sequence of events. The values of E_a and A can be obtained experimentally by determining the rate constant at several temperatures and extracting from $\ln k_{obs}$ vs. $1/T$ plot.

When applied to an elementary reaction step, E_a can be related to the threshold energy of the reaction, and the pre-exponential factor A can be related to entropic requirements imposed as the reactants convert to products. In such cases, Arrhenius

parameters for one reaction can be compared to values measured for other reactions with well-established mechanisms to provide information on the nature of the chemical processes.

Most techniques used to extract elementary rate constants rely on the use of dilute reagents and small reaction extents. In the condensed phase, this usually means measuring the initial rates and products of a reaction with a large excess of liquid solvent. Imagine an acidic species and a compound that can undergo an acid-catalyzed reaction. Both of them are surrounded by a very dense layer of solvent molecules, their salvation shell. The probability that two reagents will encounter each other by their random motions through the fluid is low, and to initiate the reaction they must have the correct relative orientation so that internal motions of the complex lead to a transition state, then to products. The solvent shells must fit this close interaction so that a chemical reaction can happen. Once the complex has been generated, its reaction followed by separation of the (solveated) products must be energetically favorable relative to simple separation of the complex back into the initial reactants. Because their concentrations are very low, products can be assumed to be inactive toward further reaction.

However, in photoresists, reactions take place in the solid phase, with actually no solvent, and usually are carried out until large proportions of the reactants are reacted. Consider how the acid-catalyzed process will be different when the acid functions on the same functional group attached to a chain within a solid polymeric resist film. First, the

concentrations of reactants and products typically are much higher than in solution, and the secondary reactions considered previously to be negligible in dilute mixtures can have a significant impact. Specific relevant examples include the detection of an unexpectedly complex mixture of volatile products formed during PEB of an exposed positive-tone chemically amplified resist and the identification of foreign polymer structures in chemically amplified resist films following PEB. Second, compared to the solution state, in a polymeric environment, molecular mobility is much reduced, and this can influence, for example, the encounter rates of reactants and the separation rates of nascent products, and can restrict the relative orientations of reactants that can be achieved in the encounter complex. In consideration of these factors, it is expected that catalysis rates and product distributions occurring in a polymer film will not be identical to those measured for the same reactants present in solution as small molecules and at low concentrations.

Because the illuminating light intensity will not be distributed uniformly inside the resist film, the acid catalyst is produced in the resist film is spatially non-uniform, and there are initial gradients in local concentrations of the photoproducts. As the PEB process goes on, the spatial distributions of acid catalyst, reactants, and products evolve in a complex manner, transforming the initial image. One of the processes affecting the final image is diffusion.

At the microscopic level, the diffusion process can be regarded as a sequence of

random movements of the diffuser relative to its surrounding environments. If the diffusant is not uniformly distributed, these random movements will tend to spread the diffusant out until it is homogeneously distributed. The kinetics are described macroscopically by Fick's law,

$$j = -D\nabla C \tag{3}$$

where j is the molar diffusion flux vector, D is the diffusion coefficient, and C is the molar concentration of the diffusing species. Therefore, the diffusion rate is most strongly affected by the spatial distribution of the diffusing species, or its concentration gradient, and by the success rate of attempts at net displacement, as indicated by the magnitude of the diffusion coefficient.[2]

The diffusion coefficient is very useful to understand the microscopic detail of the reaction. Its magnitude is very sensitive to the phase of the medium (gas, liquid, or solid) of a given diffusant and to the chemical nature of the interaction between the diffusant and its surrounding atoms and molecules. As in all solids, in order to move from one place to another, an atom or molecule must have a vacant volume available. In general, such voids are created transiently in a polymer through fluctuations of the polymer chain; in consequence, the magnitude of the diffusion coefficient is determined by the size of the diffusant and on the range of motion in the polymer. When the polymer is undergoing decomposition, as in a deprotection reaction, its density changes can be large but are not instantaneous. It takes time for the small molecules formed during the reaction to diffuse

out of the film or find energetically favorable traps. Those molecules may leave behind small voids that collapse only through polymer motion. These voids, or free volume, are believed to play an important role in mediating transport through the polymer film. The value of a diffusion coefficient can also be strongly affected by experimental conditions. Typical values of the diffusion coefficient are given in Table 2.[2]

Table 2. Typical values for diffusion coefficient D.

Diffusant	Medium	Temperature (°K)	D (cm^2/s)
Gas	Gas	273—298	0.1
Polar organics	Water	298	1×10^{-5}
He	Glass	298	1×10^{-10}
Metal	Metal	298	$1\times10^{-16}-1\times10^{-20}$
Air	Polymer	298	$1\times10^{-7}-1\times10^{-9}$
Nonpolar organics	Polymer	310	$1\times10^{-7}-1\times10^{-9}$
Polar organics	Polymer	315	$1\times10^{-9}-1\times10^{-12}$
Ion pairs	Polymer	340	$1\times10^{-16}-1\times10^{-18}$

B. Introduction

As discussed in the background, during the post exposure bake step, photoacid catalyzes the deprotection reaction, in which the protecting group is cleaved and the

blocked insoluble polymer is converted to a soluble polymer with hydroxyl group and a volatile component. The volatile group then generates free volume enhancing the photoacid diffusivity. Meanwhile, the photoacid can be deactivated by neutralization, evaporation, or be trapped due to lack of free volume. The free volume decreases continuously through polymer relaxation, which results in resist volume shrinkage.[3] Some resist systems also suffer from substrate or air contamination. With the silicon device being scaled down below 65nm, the contribution of photoacid diffusion and lateral deprotection to lithographic image spreading is considerable and increases sharply as feature size decreases further. Photolithography using chemically amplified resist (CAR) to print sub-50nm features will require an overall precision of 2-5nm.[2] Considering that the future evolution of DUV, Electron Beam or Extreme UV (EUV) lithography systems will depend critically on refinements in CAR,[2] a thorough understanding of the acid diffusion and catalyzed deprotection is essential to achieving such high lithographic resolution.

Numerous methods have been reported to characterize the acid diffusion and deprotection: multi-layer structures composed of acid source–intermediate–acid detector;[4-6] measurement of line width as a function of PEB time; spectroscopic probes of polymer changes during or after PEB;[7,8] ionic conductivity.[9-11] The major issue in these methods is the difficult of separating diffusion and deprotection kinetics, which leads to large discrepancy in measured acid diffusivities. The diffusivities reported in these

literatures ranges from 0.1 to $10^3 nm^2/s$. Additional issues affecting PEB modeling and characterization include the dependence of acid diffusion on material composition and free volume, or non-Fickean diffusion, which means diffusivity continuously varies in PEB, and resist shrinkage, which increases acid and reactant concentration and therefore accelerate deprotection.[12]

During my Master's research, we develop a novel methodology of simultaneously probing the kinetics of photoacid diffusion and catalyzed-deprotection of positive-tone resists during PEB by in-situ measuring the change of impedance of resist film. Considering a capacitor with an exposed CAR film as the dielectric medium, due to photoacid produced by exposure, this capacitor has some conductance. Baking the capacitor at typical PEB temperature, deprotection reactions will cleave the protection groups and convert the resist material from non-polar to polar substance.[3,13] So the dielectric constant of the resist film will increase, which dynamically changes the capacitance. Thus the rate of change of the material composition, i.e., deprotection rate, can be extracted from capacitance change. Note that, however, the resist shrinkage must be taken into account when calculating dielectric constant from measured capacitance. Meanwhile, the acid diffusivity throughout the course of PEB can be extracted from conductance measurement using Einstein relation. The acid diffusion is not necessarily Fickean and its dependence of reaction state and free volume is extracted by comparing capacitance-conductance curve. The determination of acid diffusivity using conventional

ionic measurement method requires the knowledge of acid concentration, measurement of which is not trivial and often is of poor precision.[12] So we develop a novel method to extract diffusivity from conductance change based on the fact that the conductance depends on not only total amount of acid, but also the distribution of acid.

C. Experiment Setup

The experiment is done with positive-tone Shipley UV5 resist, whose Dill's ABC parameters and refractive index are A = 0μm^{-1}, B = 0.5260μm^{-1}, C = 0.0510cm^2/mJ, n=1.7760 [?], respectively. The resist was spun on a highly-doped p-type wafer (resistivity<0.005 Ω-cm) at 3000rpm for 60sec. No anti-reflective coating (ARC) was used. Then the wafer is soft baked (SB) at 130^{o}C for 60sec. The resist film was 630nm thick after SB. Then a 500W mercury/xenon lamp was used to flood expose the resist. The output power of this lamp at 248nm wavelength is 2.5mW. After exposure, the wafer is placed on a 60^{o}C hotplate. Then another highly-doped p-type wafer was put on top of the resist film, a 250g metal cylinder was placed on the back of the second wafer to ensure firm contact of the two wafers. A Teflon film is inserted between the metal cylinder and the wafer as an insulator. Then the hotplate was heated from 60^{o}C to the desired PEB temperature, namely 130^{o}C. The time it took for the hotplate to reach 130^{o}C was recorded, which was about 60sec, to get the correct starting time of PEB. During PEB, an Agilent 4284A Precision LCR Meter was connected to the two highly-doped

wafers to measure resistance and capacitance. The measured data were recorded once per second. The highly-doped wafers can be considered as good conductors and their impedance can be ignored. Metal conductor is not used in this experiment because it can contaminate resist.[14] Moreover, a piece of paper was placed on the hotplate to isolate the wafers and the hotplate to prevent possible short-circuit of the two wafers through the hotplate. The experiment apparatus is shown in Fig. 4.

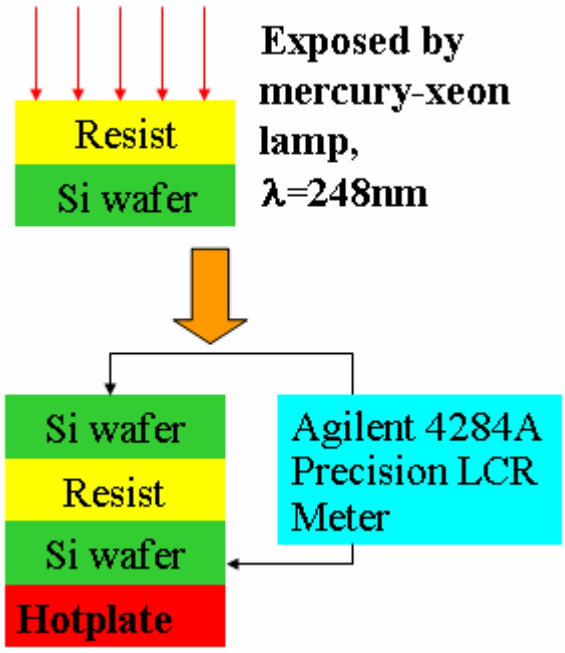

Fig. 4. Experiment setup.

The reason that we heated the hotplate after wafer and probe setup is that the nominal PEB time is 90sec, while the setup took at least 10sec. Thus it is improper to

setup the wafers and probes on 130^{o}C hotplate. On the other hand, the deprotection and diffusion rate increase exponentially with temperature, that is, the reaction/diffusion are significant only when temperature is near 130^{o}C. Given that fast heat-up rate (60^{o}C to 130^{o}C in 60sec), the reaction/diffusion having occurred before hotplate reaches 130^{o}C are negligible.

In addition, the resist thicknesses before PEB and after 30, 60 and 90sec PEB were measured.

D. Qualitative Analysis and PEB Model

Figure 5 depicts the measured RC curves, exposure dose 75mJ/cm^2, PEB 130^{o}C. The hotplate reached 130^{o}C at t=60s, when C started increasing sharply, indicating the beginning of deprotection. At the same time, R began to decrease, suggesting an increase of acid diffusivity. Our conjecture is that deprotection generates free volume that enhances acid diffusion. From t=70s, however, R began to increase, indicating that free volume was absorbed by polymer or escaped to air, and thus the acid diffusivity actually decreased because of the polar environment resulted from deprotection reactions. From t=80s to 100s, C slowly increased, indicating continuing deprotection. Meanwhile, R slowly decreased, which can be explained by the combined effects of several factors: free volume enhances but polar environment reduces acid diffusion, and resist shrinkage increases acid concentration. From t=150s, R and C were essentially constant, except for

occasional fluctuations that were believed to be due to thermal disturbance. This means the end of deprotection reaction. Note that R did not change up to t=300s, which indicates no acid loss in the PEB of UV5 resist. This agrees with the observation in Ref. 12 that CAR would be inefficient if there exists permanent loss pathways for acid because the catalytic chain length is very long, up to 1000 deprotection events per proton. In addition, the normalized resist thickness loss during PEB is plotted in Fig. 6. Obviously the thickness loss was not negligible.

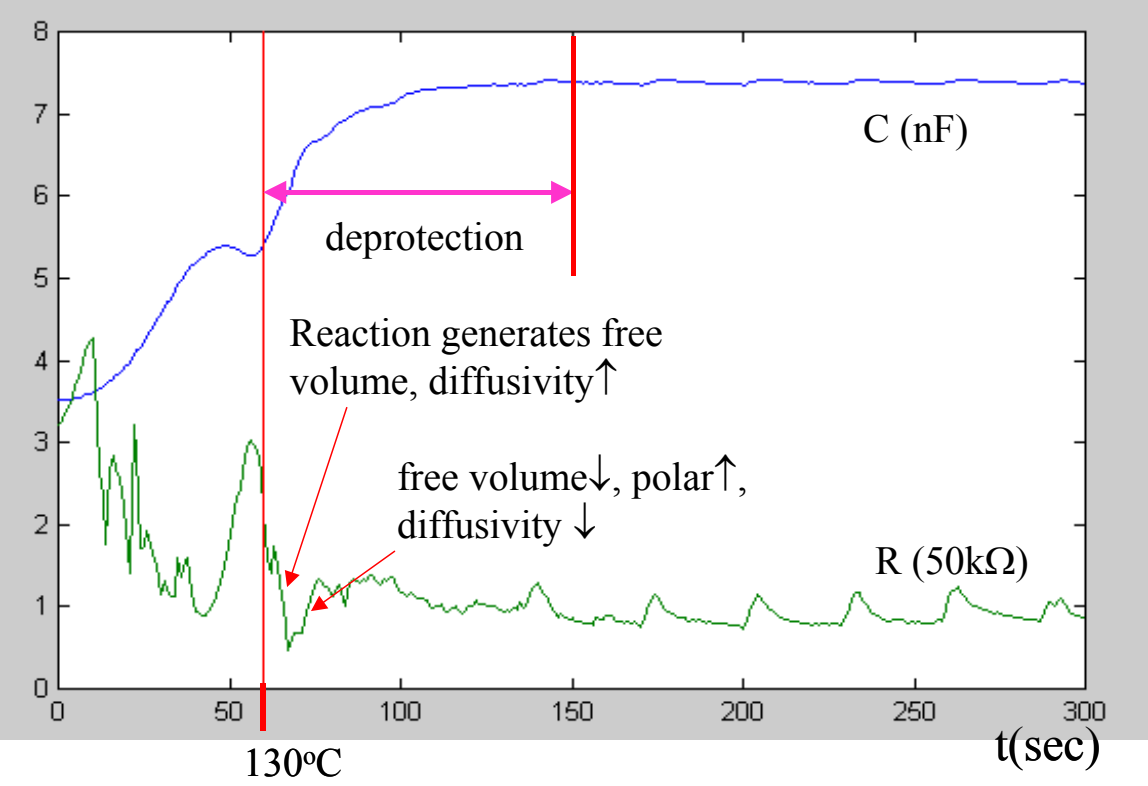

Fig. 5. RC measurement, exposure dose 75mJ/cm^2, PEB 130ºC.

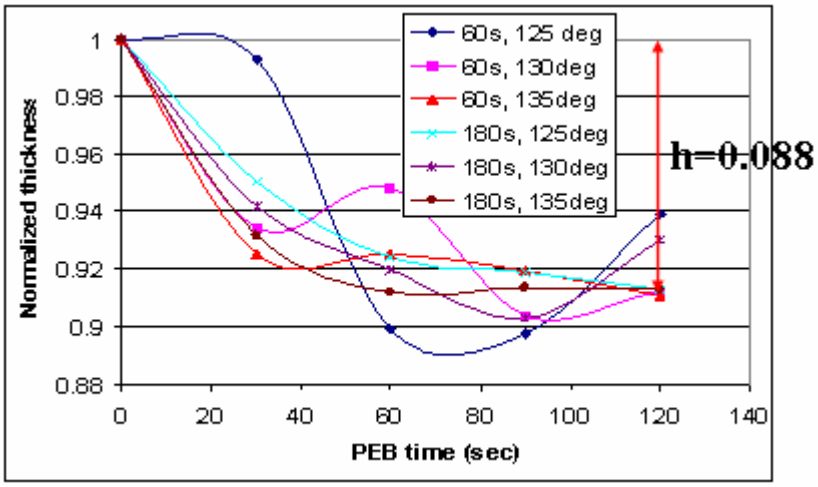

Fig. 6. Normalized resist thickness vs. PEB time. The legend represents exposure time (2.5mW/cm^2 per second) and PEB temperature.

Given the above PEB picture, a comprehensive yet succinct PEB model is proposed in this chapter, which differs from most of the previous models in that it explicitly incorporates resist thickness loss. The models proposed by E. Croffie et al.[15] and N. Jakatdar et al.[16] also describe the volume shrinkage of resist. However, their mathematical formulations involve some parameters that can not be directly measured from first principle, whereas all the parameters in this proposed model can be directly measured.

The volume shrinkage depends on the stress distribution in resist.[15] Usually the resist polymer is elastically constrained in lateral directions and free at the interface between resist and air. Thus we assume the volume shrinkage only occurs in vertical direction in the form of thickness loss. Suppose x and y coordinates are lateral direction

while z coordinate is vertical direction. Let $u = u(t)$ be the resist thickness at time *t*. Define a normalized coordinate $z' = z/u$. Thus $z' = 0$ and $z' = 1$ correspond to the bottom and top of resist film, respectively. Let $P(x, y, z')$ be the number concentration of protecting group at (x, y, z'). The actual concentration of protecting group at (x, y, z) is therefore given by $P(x, y, z')/u$. It is difficult and often unnecessary to know the actual number of protecting groups. So we denote $P(x, y, z')$ as the normalized concentration of protecting group, that is, $P(x, y, z') = 1$ and $P(x, y, z') = 0$ correspond to fully protected and fully deprotected states, respectively. Similarly, let $H(x, y, z')$ and $V(x, y, z')$ be the normalized concentration of photoacid and volatile component, respectively.

The deprotection reaction is given by

$$\frac{\partial}{\partial t}\left(\frac{P(x,y,z')}{u}\right) = -k_1 \frac{P(x,y,z')}{u}\frac{H(x,y,z')}{u} \tag{4}$$

Where k_1 is the deprotection rate constant and satisfies Arrhenius relation.

The photoacid diffusion is described by

$$\frac{\partial}{\partial t}\left(\frac{H(x,y,z')}{u}\right) = \nabla \cdot \left(D(x,y,z')\nabla\left(\frac{H(x,y,z')}{u}\right)\right) - k_2 \frac{H(x,y,z')}{u} \tag{5}$$

Where $D(x, y, z')$ is the local acid diffusivity and k_2 is the acid loss rate constant, $\nabla = \left(\frac{\partial}{\partial x}, \frac{\partial}{\partial y}, \frac{1}{u}\frac{\partial}{\partial z'}\right)$ is gradient operator.

Each deprotection event generates a volatile component and then volatile

components are absorbed through polymer relaxation, which is described by

$$\frac{\partial}{\partial t}\left(\frac{V(x,y,z')}{u}\right) = k_1 \frac{P(x,y,z')}{u}\frac{H(x,y,z')}{u} - k_3 \frac{V(x,y,z')}{u} \tag{6}$$

Where k_3 is the polymer relaxation rate constant and satisfies Arrhenius relation.

The polymer deformation depends on stress distribution, so the volume shrinkage in exposed and unexposed areas may be different. Nevertheless, in bright-field applications, the background is exposed and volatile components can evenly diffuse into and be absorbed by polymer matrix without substantial barrier. As the first order of approximation, all the exposed regions can be considered to have the same thickness loss. Suppose the absorption of one volatile component leads to a thickness loss $h \cdot u(t)$, where *h* is the ratio of the heights of one unit of normalized volatile group and the whole polymer matrix. Then the resist thickness loss at the exposed region is given by

$$\frac{du(t)}{dt} = -k_3 hu \frac{\iiint V(x,y,z')dz'dxdy}{\iint dxdy} \tag{7}$$

The acid diffusivity is enhanced by local free volume (volatile group) concentration and reduced by polar environment (deprotected site), thus it can be described by the Fujitu–Doolittle equation and deprotection induced activation energy increase:

$$D = D_0 \cdot \exp\left(\frac{w_1 V/u}{1 + w_2 V/u}\right) \cdot \exp\left(\frac{w_3 P/u}{kT}\right) \tag{8}$$

Where w_1, w_2 are constants, D_0 is the diffusivity in fully deprotected polymer

and satisfies Arrhenius relation, and w_3 is a constant describing how activation energy is altered by protecting group. If the flood exposure dose is over 225mJ/cm^2, all photoacid is released, and thus all photoacid is disturbed uniformly in the resist film. Therefore, the capacitance and resistance of the resist are given by

$$C = \frac{\varepsilon A}{d}, \varepsilon = \varepsilon_{deprotect} - \varepsilon_{protect} P \tag{9}$$

$$R = \frac{d}{\sigma A}, \sigma = \frac{q^2 DH}{kT} \tag{10}$$

Where ε is the dielectric constant of the resist which is assumed to linearly increase with protecting group P decreasing. A and d are area and thickness of resist film, respectively, and σ is the conductivity related to acid diffusivity though Einstein equation.

E. Experimental Results and Parameter Extraction

The Resistance and Capacitance versus time curves at doses 75, 150, 225 and 450mJ/cm^2 are plotted in Fig. 7.

First we can extract reaction rate constant k_1 and acid loss rate k_2. When dose is over 225mJ/cm^2, the acid concentration H=1 everywhere. Figure 6 shows that resist thickness loss can be neglected after 40sec PEB. Then we have

$$\frac{\partial}{\partial t} \ln P = -k_1 H = -k_1 \tag{11}$$

Suppose $C_1 = \frac{A}{d}\varepsilon_{deprotect}$ is the capacitance of the resist after PEB. Then from Eqs. (9)-(11), we have

$$k_1 = -\frac{\partial}{\partial t}\ln(C_1 - C) \tag{12}$$

Figure 8 plots the $\ln(C_1 - C)$ curve with linear fitting at 225mJ dose, whose slope is $k_1 = 0.0537\text{s}^{-1}$.

Since R does not change from t=150s up to 300s, there is virtually no acid loss, i.e., $k_2 = 0$.

Then we can extract h, the thickness loss induced by a unit of volatile group. The total number of volatile groups absorbed during PEB is 1 unit. So h is simply the reduction of normalized resist thicknesses due to infinitely long PEB. From Fig. 6, we can easily find that $h = 0.088$.

We then extract w_3, the dependence of diffusivity on deprotection level from R. There is no free volume both at the beginning and at the end of PEB, so D can be written as

$$D = D_0 \exp\left(-\frac{E_D - w_3 P/u}{kT}\right) \tag{13}$$

At the beginning of 130°C PEB, $t = 0, P = 1, u = 630 \pm 13nm$; at the end, $t = \infty, P = 0, u = 573 \pm 12nm$. From Eqs. (8)-(10), we have

$$w_3 = kT \ln\left(\frac{R(t=\infty)/u(t=\infty)}{R(t=0)/u(t=0)}\right) \tag{14}$$

As is shown in Fig. 9, w_3 =5.56×10^{-3}eV.

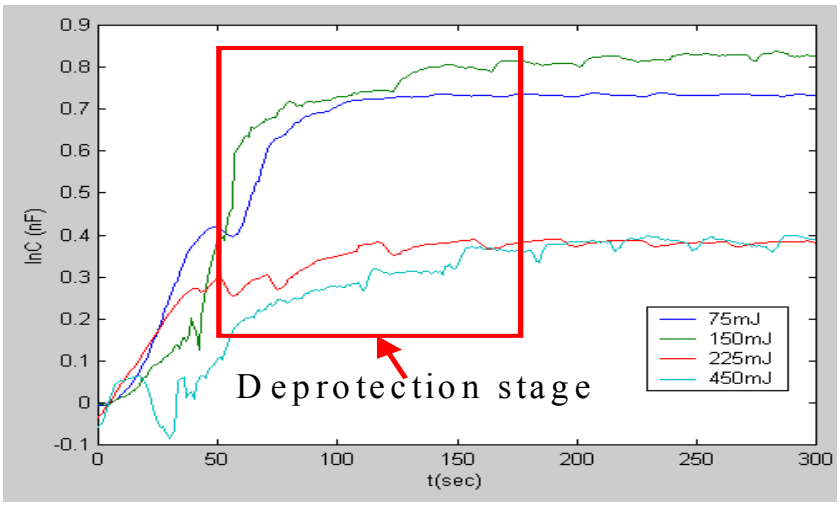

(a)

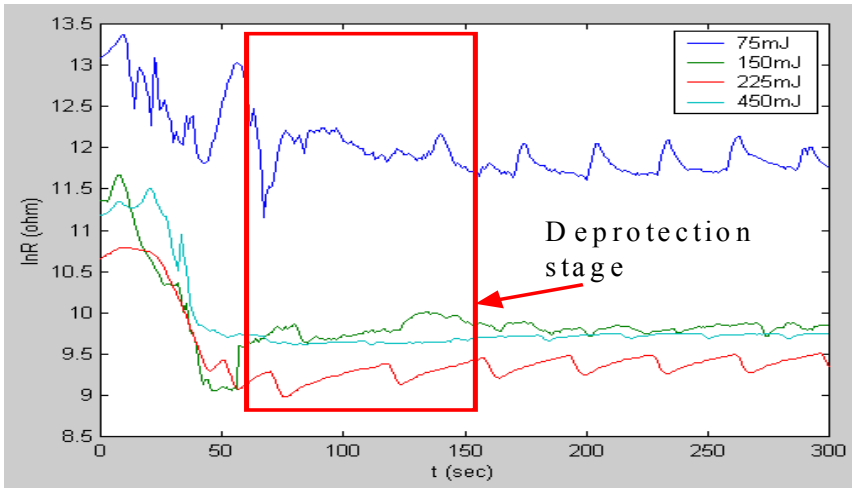

(b)

Fig. 7. Capacitance and resistance variations during PEB (a) Capacitance (b) Resistance. Note that C and R are in log scale. The legend represents exposure dose.

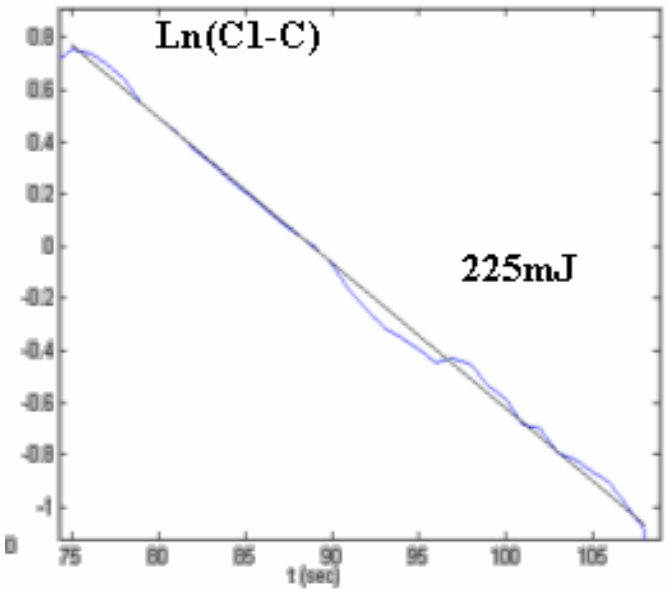

Fig. 8. Extracting reaction rate constant k_1 from ln(C_1-C) vs. t. The slope is k_1.

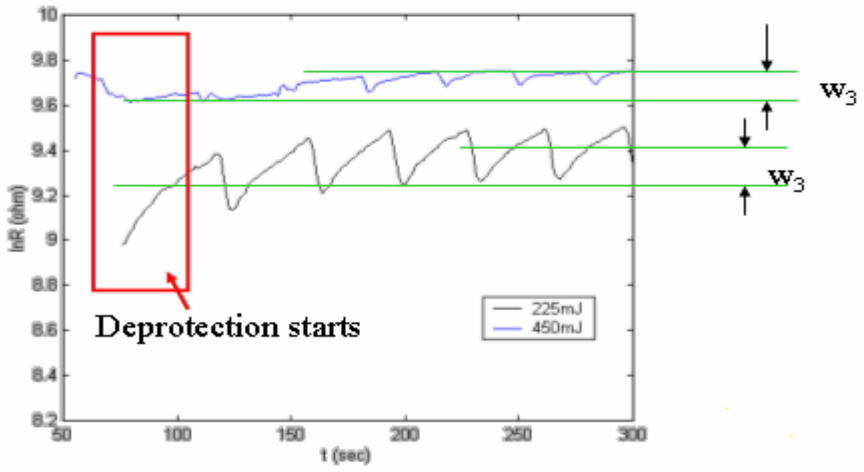

Fig. 9. Resistance variation in 130°C PEB.

In order to extract the parameters w_1, w_2 and k_3, the parameters of enhancement of acid diffusivity by free volume and polymer relaxation constant, we can solve the partial

differential equation (PDE) system Eqs. (10)-(16) with the extracted parameters k_1, k_2, w_3 and h, and then fit the simulated R and C with the experiment data. By minimizing the RMS error between simulation and experiment, the parameters can be extracted. The experimental dose of dose 225 and 450mJ/cm^2 were chosen because in these two cases, acid is uniformly distributed. Time-domain finite difference (TDFD) method was used to solve the PDE system. It is found that as long as k_3 is large enough, the simulation is very accurate (RMS error<0.1%) and insensitive to variation of w_1 and w_2. This means that the free volume is absorbed by resist in very short time (<<1sec), and thus its effect on diffusivity is not observable in the time-scale of nominal PEB. This agrees with the common assumption that polymer relaxation is rapid.[12] The simulated and experimental RC curves are compared in Fig. 10.

Finally, we can extract diffusivity D_0 from R variation. Although D can be calculated from R through Einstein equation, the measurement of the acid concentration [H^+] often has poor precision.[12] Here we presented a more robust and accurate approach. Consider the photoacid distribution in the vertical direction of the resist film resulted from exposure of 75mJ/cm^2 dose. Denote the distribution as $H(z)$, which is calculated from Dill's ABC model and is plotted in Fig. 11. Apparently standing wave effect exists for this dose. Then the resistance is given by

$$R = const \cdot \frac{1}{D} \int \frac{1}{H(z)} dz \tag{15}$$

Where *const* is an unimportant constant. Define $m(z) = 1/H(z)$. Using the 1-dimensional form of Eq. 5, and assuming the effects of deprotection level and resist shrinkage on *D* can be ignored at the beginning of PEB, we have

$$\frac{d}{dt}\ln R = D\frac{\int\left(-\frac{2}{m(z)}\left(\frac{\partial m}{\partial z}\right)^2 + \frac{\partial^2 m}{\partial z^2}\right)dz}{\int m(z)dz} \tag{16}$$

Note that Eq. 16 is only true at the beginning of PEB. Thus the diffusivity can be calculated D_0 = 9.67nm^2/s, at 130ºC. This value is close to SEMATECH measurement and agrees with literatures based on ionic-measurement or molecular simulation.[2,10,11,12] In fully deprotected resist,

$$D = D_0 * \exp(-w_3/\mathrm{kT}) = 6.56\mathrm{nm}^2/\mathrm{s} \tag{17}$$

F. Conclusion

This chapter presents a novel methodology of simultaneously measuring the non-Fickean acid diffusivity and deprotection rate in positive CAR by monitoring impedance change during PEB. The capacitance change is due to deprotection that converts non-polar polymer to polar, and the resistance is related to acid diffusivity with Einstein relation. Meanwhile, resist thickness loss has to be taken into account in modeling PEB. A comprehensive PEB model is proposed that includes deprotection reaction, free volume generation, resist shrinkage and acid diffusion which is enhanced

by free volume but reduced by polar environment.

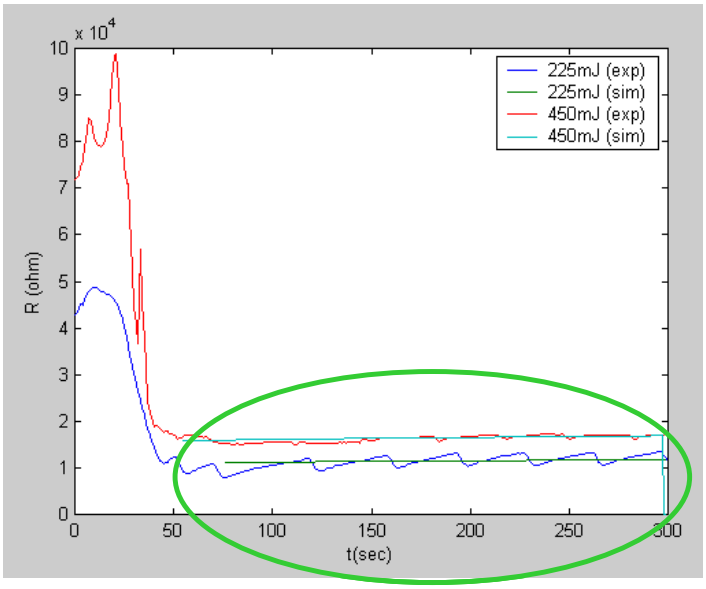

(a)

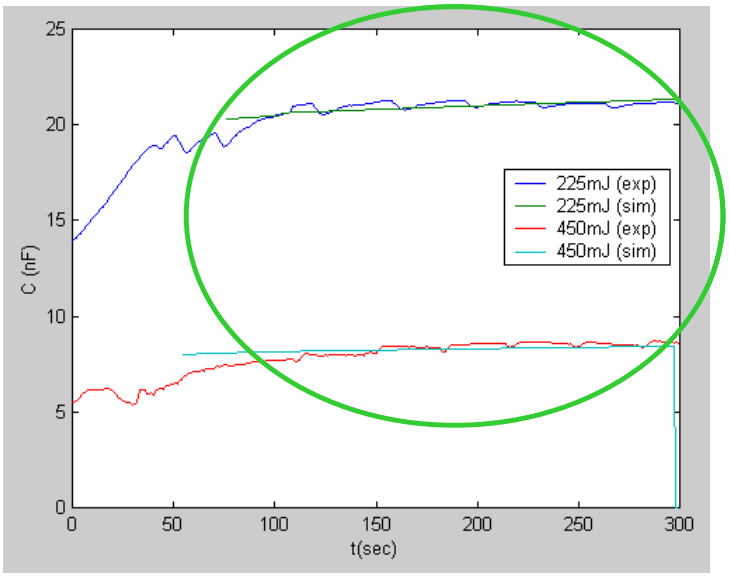

(b)

Fig. 10. Simulated and experimental RC curves, (a) R, (b) C at PEB 130ºC. In the legends, “exp” and “sim” correspond to experimental and simulated data, respectively. The curves in the green circle were used to fit simulation with experiment.

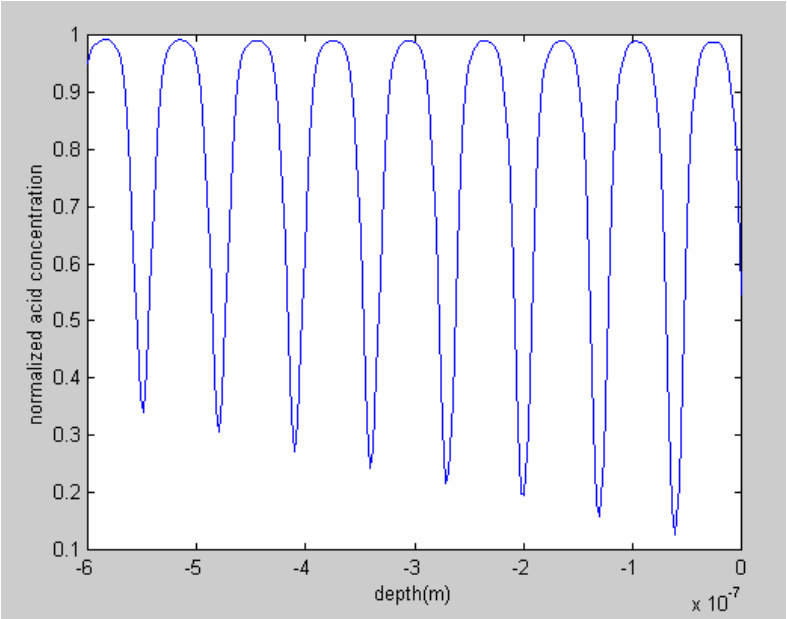

Fig. 11. Normalized photoacid concentration, dose 75mJ/cm^2.

The experiment was done with Shipley UV5 resist and all the model parameters are extracted from RC curves by using divide-and-conquer strategy. In particular, deprotection rate constant, dependence factor of diffusivity on deprotection level and diffusivity are calculated from log slope of RC curves, so they are free of measurement errors other than RC. For example, other characterization methodologies usually require measuring deprotection level or acid amount with spectroscopic methods, which often have poor precision. Some methods measure resist loss after developing, while developing mechanisms are not well understood yet. So our methodology is supposed to be very accurate.

It is found that free volume escapes to air or is absorbed by polymer at a very rapid

rate, indicating that free volume enhancement of acid diffusion or reaction is negligible. Nevertheless, resist experiences continuous reduction of thickness during PEB (ultimate loss is 8.8%), which increases protecting group and acid concentration and therefore increases deprotection rate. In UV5, acid diffusivity is 9.67nm^2/s in fully protected resist and 6.56nm^2/s in fully deprotected. Although particle diffusivities in polar and non-polar environment usually differ by 1~3 orders of magnitude, this 50% difference can be explained by the fact that protection level is usually 20-30% in CAR and thus the polarity change due to deprotection is not dramatic. The extracted diffusivity agrees with the previous work considerably well. The simulated RC curves fit experimental data very well with an RMS error less than 0.1%, indicating high accuracy of our methodology.

CHAPTER III

IMPROVING RESOLUTION AND DEPTH-OF-FIELD IN NEAR FIELD OPTICAL PATTERNING VIA LIQUID IMMERSION IMAGING

In this chapter, a novel lithographic technique, liquid immersion contact lithography (LICL) is presented and the simulations are performed to illustrate its main features. While the liquid immersion effect is not very promising for dense gratings, significant depth-of-field (DOF) enhancement can be achieved for large pitch gratings with deep-UV light (λ=248nm) illumination with both TM and TE polarizations. The improvement is believed to be due to the extra transmitted diffracted high energy high order components after liquid immersion. Better than 100nm DOF can be achieved by this method for printing 70nm aperture. The simulation results show good perspective for the application of this technique to scanning near field optical microscopy (SNOM).

A. Introduction

High sub-wavelength resolution is believed to be achievable by near field optical lithography after the demonstration of $\lambda/40$ resolution of scanning near field optical microscopy.[17] A number of near field patterning techniques to extend the resolution of optical lithography have then been reported. These include interferometric lithography,[18,19] phase shift masks (PSMs),[20,21] light-coupling mask,[22] and step and flash

imprint lithography.[23] The details of these techniques will be described below.

1. Interferometric lithography

Generally, in an interferometric lithography system, two coherent light beams are incident on a substrate to form a standing wave pattern.[18] If the angle between the two incident beams is 2θ, then the period of the sinusoidal pattern is given by

$$d = \lambda / 2\sin\theta \tag{18}$$

The modulation of the intensity is given by the fringe visibility

$$\mu = (I_{\max} - I_{\min})/(I_{\max} + I_{\min}) \tag{19}$$

where $I_{\max}$ and $I_{\min}$ are the maximum and minimum light intensities in the stand wave pattern. Fringe visibility depends on the degree of coherence between the two interfering beams and their relative strength. If the beams have equal strength and are perfectly coherent, then complete destructive interference occurs at the nodes, i. e., $I_{\min} = 0$ and a fringe visibility of $\mu = 1$ can be obtained.

With the development of lasers with excellent coherent properties, interferometric lithography techniques have become more and more powerful. Interferometric lithography is commonly used for patterning of large area gratings as it is suitable to applications that require one or two dimensional periodic patterns.[18] Some of the major advantages of interferometric lithography are its simplicity compared to imaging systems, extremely large depth-of-focus, and the tenability of the fringe pitch by changing the

angle between the beams.[19]

The ultimate resolution in an interferometric lithography system is achieved when the two beams are traveling in opposite direction to each other. In this case the period of the pattern is equal to half of the incident wavelength. For example, 100nm period line/space pattern using 193nm ArF laser light in an achromatic interferometric scheme has been obtained.[18]

2. PSMs in contact printing

The geometry of the optical system of PSM is shown in Fig. 12. Consider light passing through a transparent mask (Fig. 12). The phase, $\varphi(x)$, of light with wavelength λ that emerges from the mask is related to the relief of the surface of the mask, $u(x)$, and to the difference between its refraction index and that of the surroundings, Δn, by

$$\varphi(x) = \frac{2\pi}{\lambda}\Delta n \cdot u(x). \tag{20}$$

If we neglect the finite thickness of the relief on the surface of the mask, the electric field just after emerging from the mask (at position $z = 0^+$) can be related to the electric field just before emerging from the mask (at position $z = 0^-$) by

$$E(x, z = 0^+) = E(x, z = 0^-)\exp[i\varphi(x)] \equiv E(x, z = 0^-)\tau(x). \tag{21}$$

Eq. 21 defines the transmission function of the phase mask, $\tau(x)$.

When the relief of the surface is binary and has magnitude u_1 and periodicity d, then $\tau(x)$ can be described by

$$\tau(x) = \begin{cases} \exp(\frac{2\pi}{\lambda} u_1 \Delta n) & md < x < (m+\frac{1}{2})d, \quad m = \ldots -1, 0, 1, \ldots \\ 1 & otherwise \end{cases} . \tag{22}$$

When $u_1 = \frac{\lambda}{2\Delta n}$, the phase shift is equal to π, and the electric field undergoes abrupt changes in sign at the edges where the phase shift occurs. Since the electric field is continuous in the photoresist, these changes in sign induce nulls in the intensity near the surface of the mask This effect is the basis for generating contrast with masks that manipulate only the phase of the light.[20]

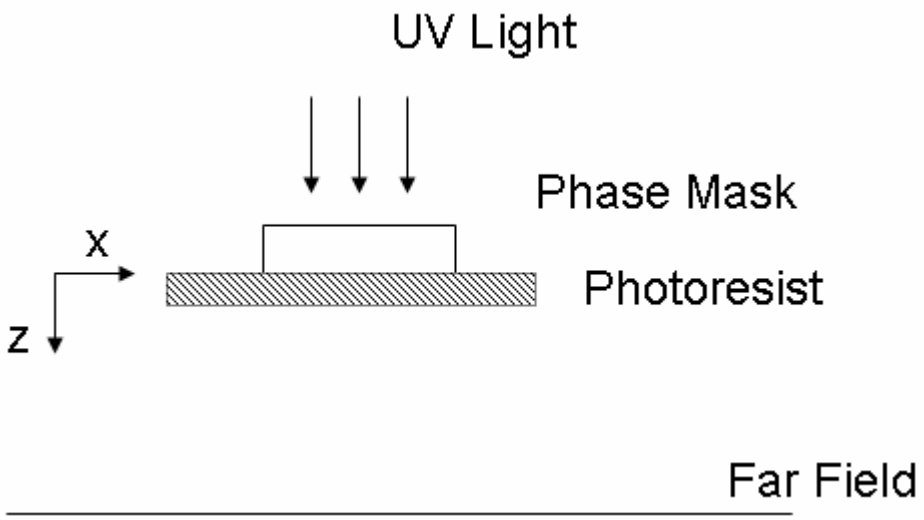

Fig. 12. Geometry of the optical system.

In the Fraunhofer regime, Fourier transformation of the transmission function, $\tau(x)$, yields the far field diffraction pattern. For a mask with periodicity *d*, diffracted orders in the far field appear at angular locations defined by

$$\sin(\theta_m) = \frac{m}{d}(\frac{\lambda}{n}), \quad m = \ldots -1, 0, 1 \ldots \quad . \tag{23}$$

In this equation, the refraction index of the material in which the light passes as it emerges from the mask is n, and λ is the wavelength of the light in vacuum. The order of the diffraction is m.

Figure 13 illustrates the patterns of intensity in the near and far fields for binary phase masks that induce shifts of the phase between 0 and π. As the phase deviates from π, the amount of light that appears in the zeroth order in the far field increases. This increase corresponds to a reduction in the contrast in the near-field pattern.[20]

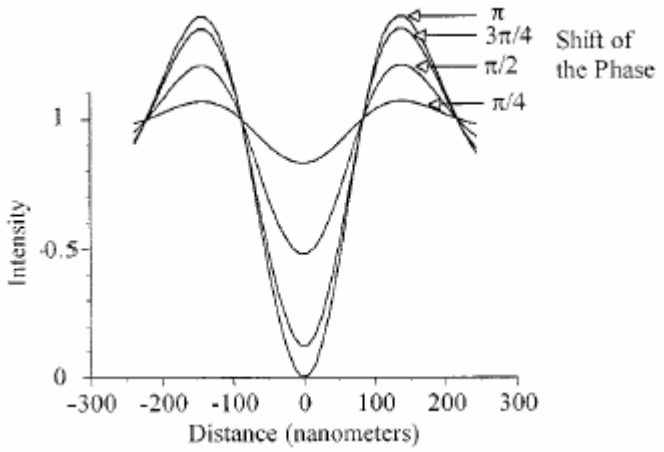

Fig. 13 Variation of the pattern intensity as a function of the shift of the phase.

3. Light-coupling mask

Figure 14 shows a light-coupling mask scheme. It uses a structured polymer to contact the resist. This polymer is able to make a conformal contact with the substrate

because it can accommodate small height variations on the substrate without damage to the substrate or polymer so that the light-coupling mask can be used many times without suffering mechanical wear.[22]

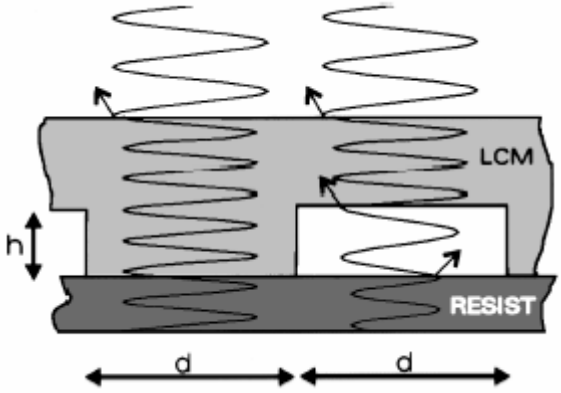

Fig. 14. Schematic of light passing through a structured polymer in contact with a resist.

In a light-coupling mask, the light comes from the above and the refractive index of the light-coupling mask is the same as the resist below. The matrix causes a blueshift, which is proportional to the refractive index of the polymer in the effective wavelength of the traveling wave, when the light enters a light-coupling mask (as depicted in Fig. 14). The path of light is significantly changed as the wave front encounters the boundaries in the mask. The degree of change and the principal cause of contrast in the intensity of light are determined by the boundary and its dimension relative to the wavelength λ in the polymer .[22]

4. Step and flash imprint lithography

In the step and flash imprint lithography process, an organic transfer layer is coated on a silicon substrate by spinning. A transparent template with relief structures of a circuit pattern is closely aligned over the coated silicon substrate. Once in proximity, a drop of a low viscosity, photopolymerizable, organosilicon solution is introduced into the gap between the template and the substrate. The organosilicon fluid fills the gap by capillary action. The gap is closed when the template makes contact with the transfer layer that is coated on the substrate. Once in contact, the structure is irradiated with ultraviolet light through the backside of the template. Ultraviolet exposure cures the photopolymer and creates a solidified, silicon rich, low surface energy replica of the template. Once the photocuring is complete, the template is separated from the substrate, leaving a relief image on the surface of the coated substrate. An oxygen-RIE (reactive ion etching) etch through the transfer layer is used to create a high aspect ratio image on the substrate. This process is conducted at room temperature, and since the template is transparent, all of the alignment schemes that have been used successfully in mask aligners can be implemented without difficulty. The processes required to create the image are depicted in Fig. 15.[23]

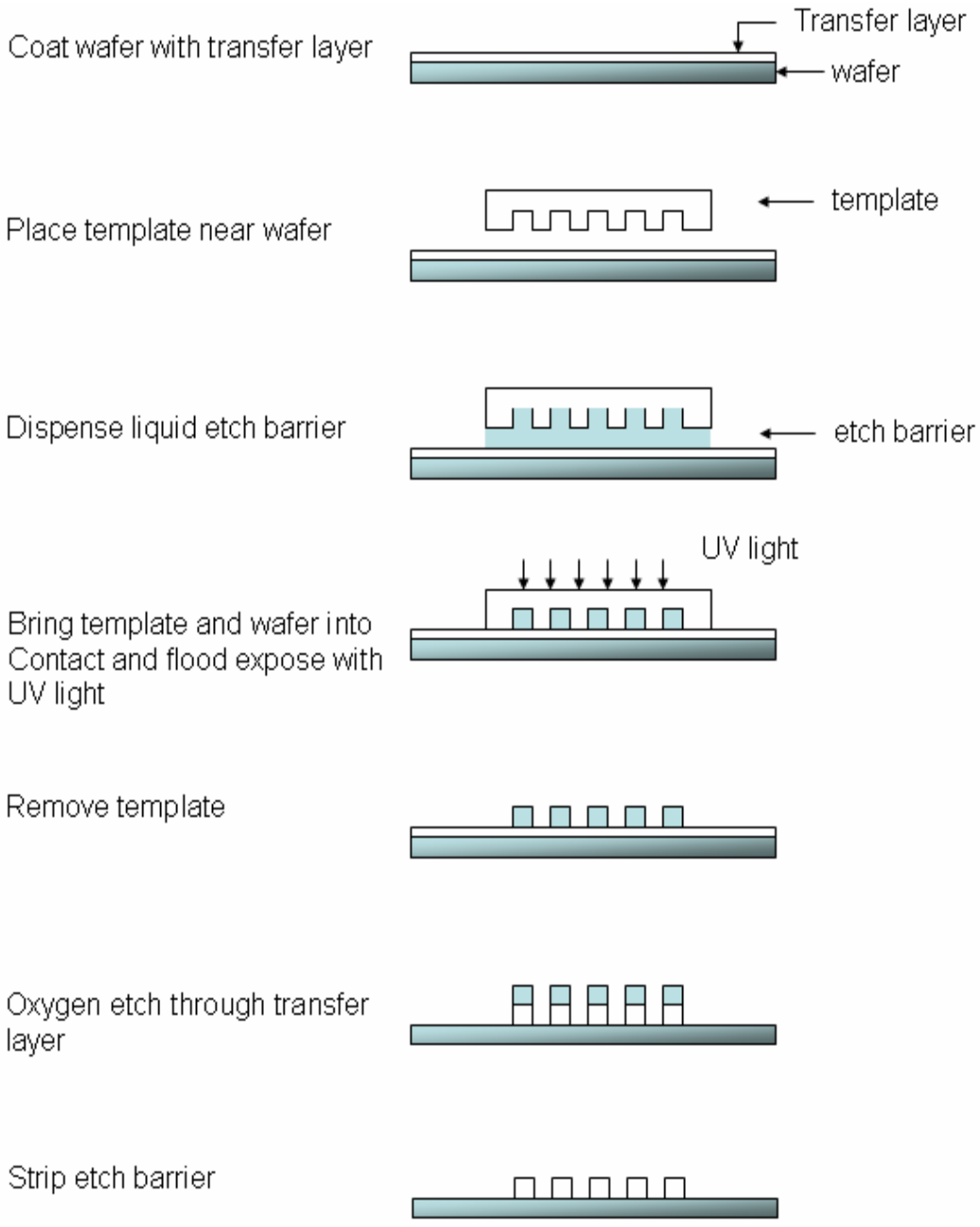

Fig. 15. Step and flash lithography process sequence.

All these near field optical methods described above can be categorized as dry contact lithography (DCL). Among these lithography techniques, the DOF is very small

when printing sub-100 nm patterns, usually less than 100nm. So an ultrathin photoresist film is necessary in such applications, which poses difficulty to the next etching step.

Liquid immersion lithography (LIL),[24] which uses liquid immersion to decrease the effective wavelength of the incident light, is an inexpensive method to improve the resolution and the DOF. Extending this technology to contact lithography will obtain the same advantages and, meanwhile, rid the need of very expensive lens. In my research, we develop a novel lithographic technique, liquid immersion contact lithography (LICL). Simulations are performed for the grating mask suspended in air (corresponding to conventional contact printing) and immersed in liquid, to investigate the impact of liquid immersion on the diffracted near field. Small and large dimensions of grating pitches are simulated to explore the effect of liquid immersion in printing dense lines as well as isolated line.

B. Simulation Methods and Models

In this research, we used TEMPEST, a computer program developed by UC Berkeley that solves Maxwell's equations using a time-domain finite-difference (TDFD) algorithm.[25]

Our goal is to investigate the effect of liquid immersion to the diffracted near field of a chromium mask. The system geometry for simulation in Cartesian coordinate is shown in Fig. 16. A chromium transmission grating with pitch p and thickness t is on the

surface of the glass. The incident light is in *–z* direction, and the exit plane of the chromium grating locates at *z=0* plane. The chromium grating and the glass are both suspended in a medium with refractive index *n*. Simulations for both TE and TM illumination cases are performed in order to examine the impact of liquid immersion under different polarization conditions. In our simulation, we select water to be the liquid immersion medium. Simulations for large grating pitch with small aperture width are also performed to investigate the change of the diffracted near field in liquid immersion condition for printing the isolated aperture which may be used in scanning near field optical microscopy (SNOM).

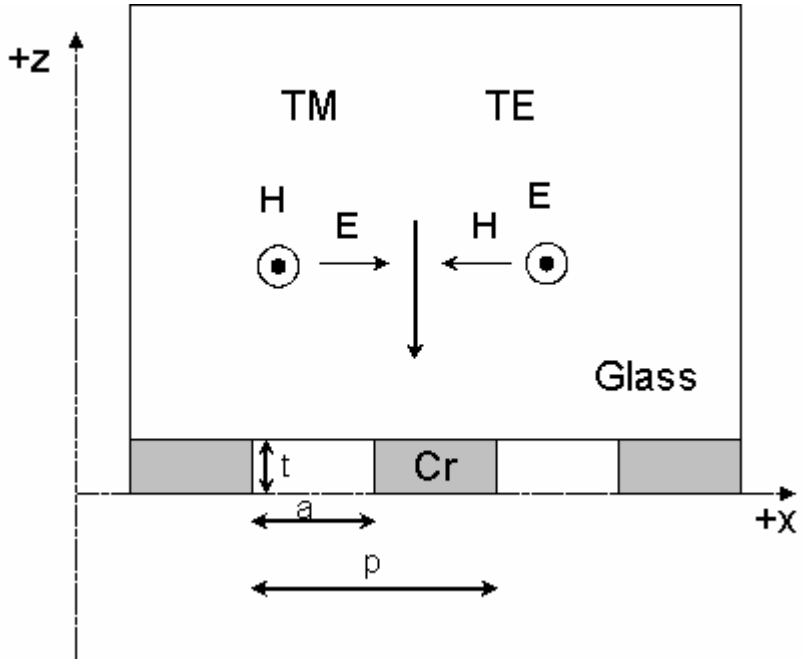

Fig. 16. Geometry of the grating system. The chromium grating on the surface of the glass has 140nm pitch, 80nm thickness. The aperture width is 70nm. The grating is illuminated by 248nm wavelength light. The light travels in –z direction.

C. Results and Discussions

1. Dense line

The two-dimensional near field intensity profile is shown in Fig. 17, for a 140nm pitch grating with Cr conductors (n = 0.85, k = 2.01),[26] 80nm thick with a glass (n = 1.5) substrate immersed in liquid (water with n = 1.395).[26] The grating is illuminated by deep-UV light (λ=248nm) with normal incidence from the glass side. Both TE and TM polarization are simulated. Figure 18 illustrates the near field intensity of the grating with the same exposure condition as Fig. 17. Plots are extracted at z=-10, -20, -50, -100, which is 10, 20, 50, 100nm away from the exit plane. The light intensity is defined as $I(x,z) = E^2(x,z)$, where $E(x,z)$ is the total electrical field.

(1) Field enhancement

The field is intensified at the corners of the grating for TM polarization, which is believed to be due to the high electrical fields that are generated at the corners of the metal grating. The TE polarization does not have the same intensification because the majority of the electrical field is in y direction and hence does not see this sharp edge.[27]

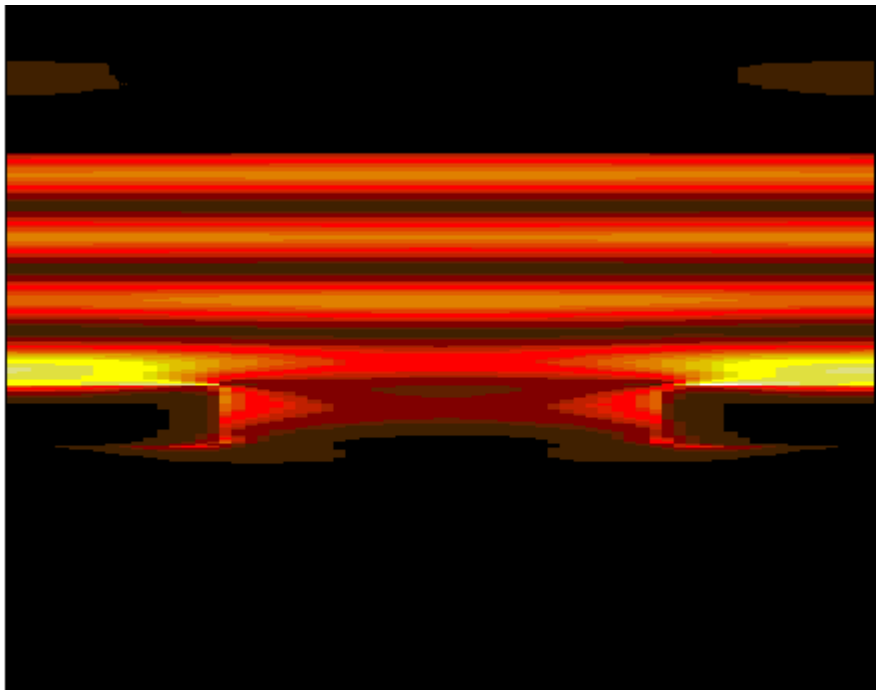

(a)

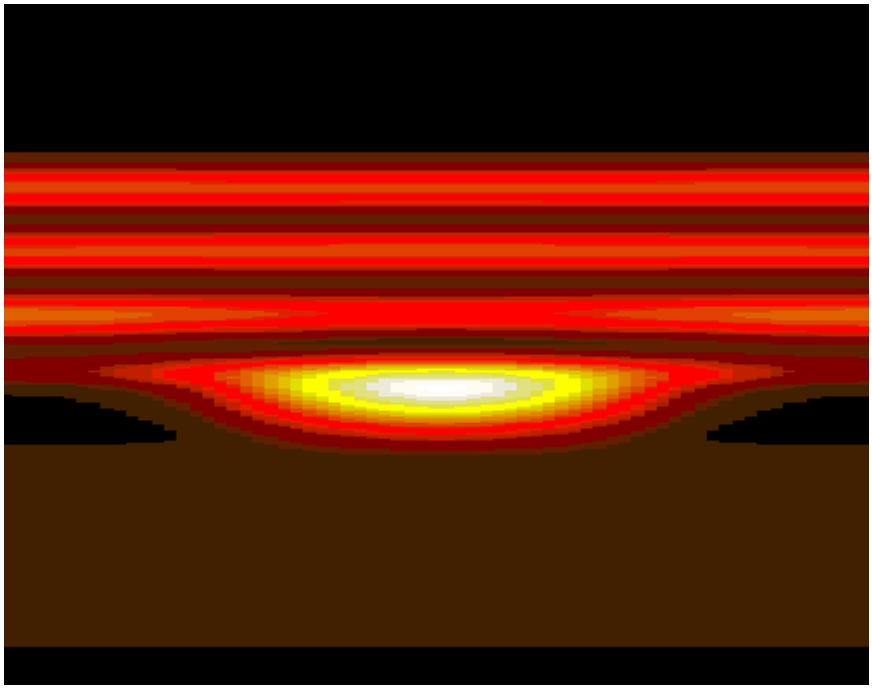

(b)

Fig. 17. Light intensity profile for 140nm grating immersed in liquid with TE and TM polarized light of 248nm illumination (a) TM polarized (b) TE polarized.

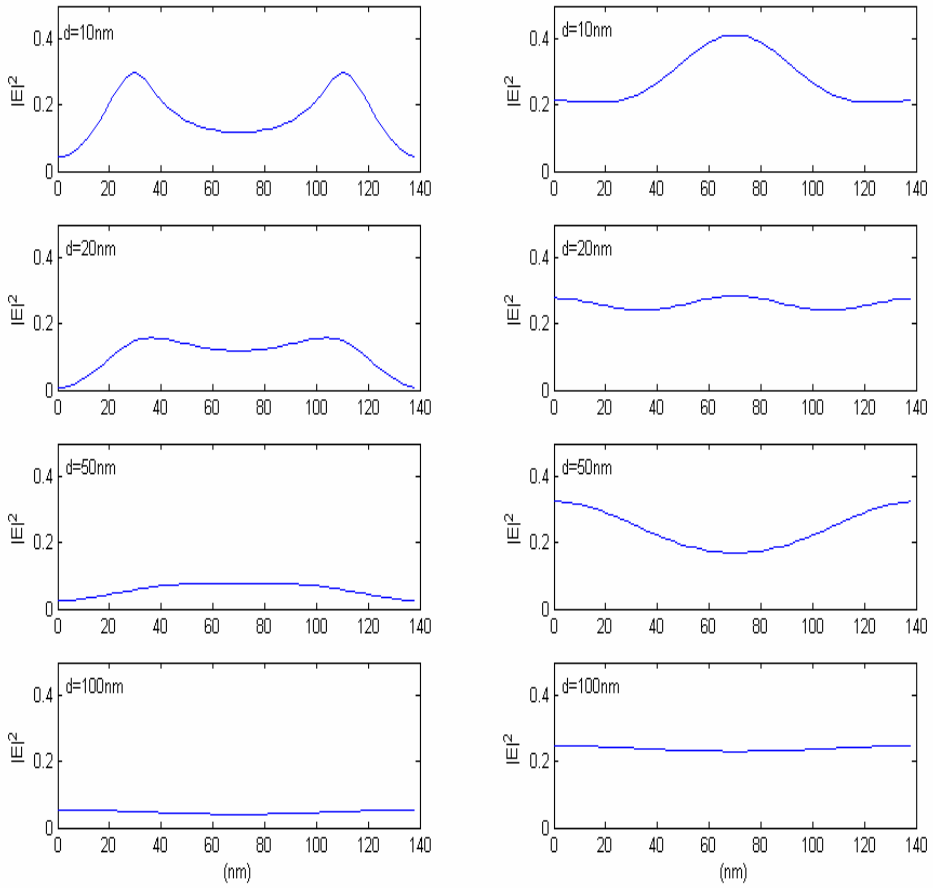

Fig. 18. Intensity line plots of same exposure condition as Fig. 17. The four plots on left hand side are TM polarized, and the four plots on right hand side are TE polarized.

With TE illumination, the light intensity that goes through the grating suspended in air is larger than the intensity goes through the grating immersed in water, whereas with TM illumination, the situation is on the contrary. This is because that for TE polarized light, the main effect of the water immersion is to reduce the effective wavelength, while the transmitted light intensity is proportional to $(\frac{a}{\lambda})^4$, where a is the dimension of the

aperture and λ is the wavelength the incident light.[28] But for TM polarization, a large part of transmitted field energy is concentrated around the corners due to Surface Plasmon (SP) resonance.[29] After liquid immersion, since the difference of the dielectric constant between liquid and chromium is smaller than that between air and chromium, the discontinuity of the dielectric constant seen by TM polarized light is virtually reduced. So in this case, the intensification effect is less severe than in air, and so does the light intensity.

(2) DOF of dense lines

To see the improvement of the liquid immersion, we have calculated the image log slope (ILS) and contrast of the transmitted field at each distance within 100nm from the exit plane of the grating. The critical dimension (CD) to be printed is chosen to be 70nm, which is equal to the width of the aperture. Then ILS is given by

$$ILS = \left. \frac{d(\ln I(x))}{dx} \right|_{x=x_0} \tag{24}$$

where x_0 is the point at the edge of the aperture. The definition of the contrast, following that used by S. J. McNab et al, is

$$c = \frac{I_1 - I_2}{I_1 + I_2} \tag{25}$$

where I_1 is the light intensity at the center of the aperture, and I_2 is the light intensity at the center of the chromium.[27] Note that this definition is different from conventional

definition of contrast, which is $\frac{I_{\max} - I_{\min}}{I_{\max} + I_{\min}}$, because for TM illumination, the maximum intensity usually occurs at the corner of the aperture, not the center. Figure 19 shows the variation of the image log slope and the contrast with respect to the distance to the exit plane, for both TE and TM polarization with 248nm wavelength light illumination. For TE polarized illumination, although the ILS and the contrast is improved within the first 10nm, ILS difference between air suspension and liquid immersion is almost not visible after a short distance because for both air and liquid cases, the contrast drops below 0.2 after 15nm. While for TM polarized illumination, the contrast and the ILS for grating immersed in the liquid is good (>0.01) after a short distance of about 20nm from the exit plane and becomes better than that for grating suspended in the air after 40nm from the exit plane of the grating. To quantitatively see the improvement, in this chapter we define depth of field (DOF) as the distance at which the ILS drops below 0.01, which means the printed line width will vary by 10nm if there is 10% variation of incident light intensity. From the value of the DOF, we can see slight improvement of liquid immersion for either TM or TE polarized illumination. The reason of this will be explained in details in the next part.

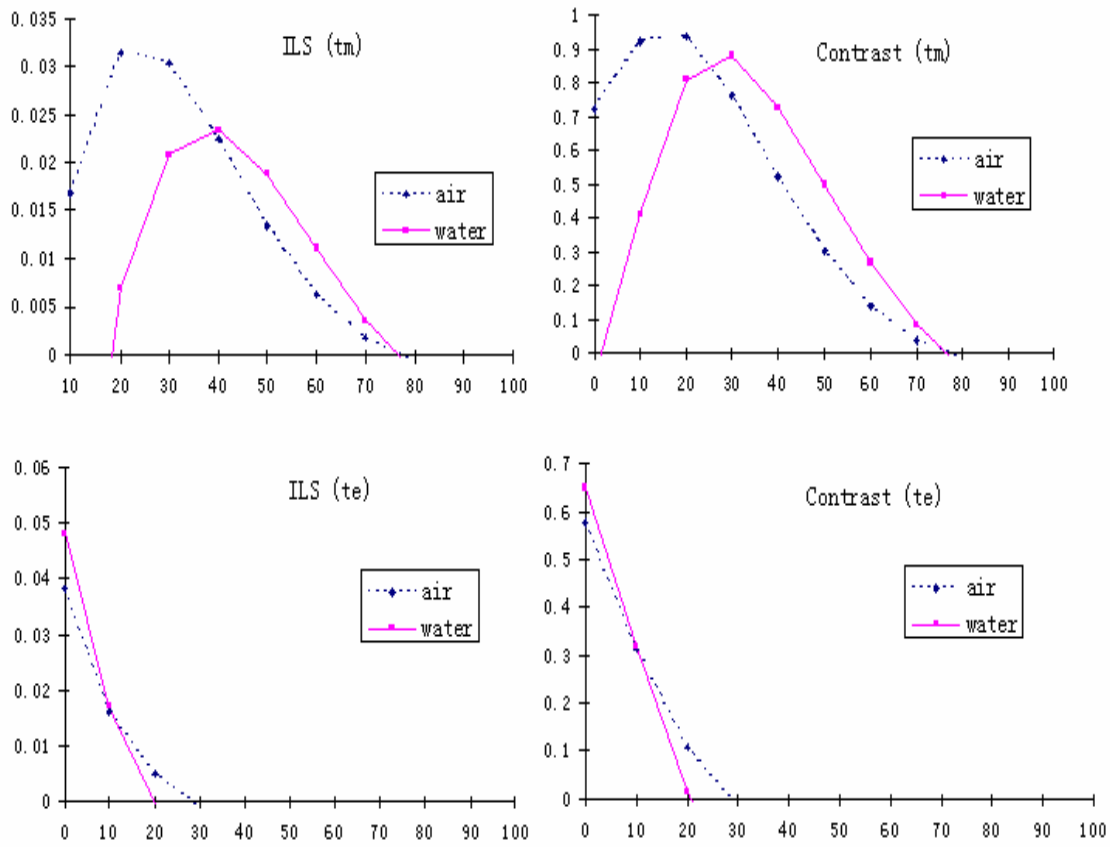

Fig. 19. The ILS and the contrast of the diffracted near field versus the distance from the exit plane of the grating. The ILS at the exit plane for TM illumination is not presented in the plot. The value at the exit plane is always much larger than other places due to the corner intensification effect. The negative values of the contrast and ILS are only present at the first several nanometers, and will not have much effect to the printed pattern. So when calculating DOF, we neglect that part.

2. Isolated aperture

Simulation for various grating pitches with fixed aperture width (70nm) shows the liquid immersion will improve DOF significantly for either TE or TM polarized illumination at 248nm wavelength. Figure 20 plots the DOF versus the grating pitch for TE and TM polarization. The improvement of DOF is not significant at small grating

pitch, which can also be observed in the foregoing discussion, but becomes much more significant at long grating pitch. The improvement for DOF is over 100% for large pitches.

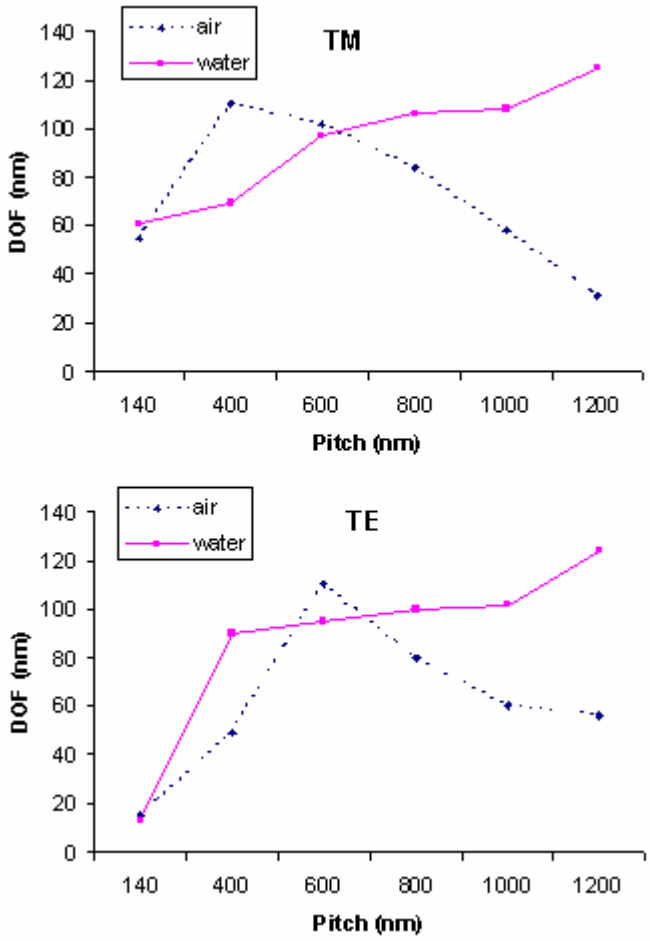

Fig. 20. DOF vs. pitch p for simulated gratings plots for TM and TE polarized illumination.

(1) Improvement of DOF

The improvement of the DOF brought forth by liquid immersion can be

qualitatively understood by considering the decay depth of the evanescent field after sub-wavelength apertures. The depth at which each diffracted component decays to $1/e$ of its initial intensity, y_m^I, is given by

$$y_m^I = \frac{1}{4\pi\sqrt{\frac{m^2}{p^2} - \frac{n^2}{\lambda^2}}} \tag{26}$$

where m is the diffracted order.[30] For low order diffracted component, y is an imaginary number, which means the diffracted component is a transmitted wave instead of an evanescent wave. In liquid immersion, the effective wavelength λ is reduced by a factor of refractive index, which means the number of transmitted diffracted components is increased. Since the aperture width is much smaller than the grating pitch, the high order components carry significant amount of energy. So with liquid immersion, the energy carried by the added diffracted components is the dominant factor for the image contrast. Because of the apodization effect resulted from the high order components, we can expect the ILS to be better. While for small p, the added diffracted components by liquid immersion are still low orders and the amount is small, so DOF is not improved in this region.

(2) Trend of DOF

Except the narrow pitch region where the difference of DOF between suspended in air and liquid immersion is not significant, there is a decreasing trend with the increase of pitch for the DOF with grating suspended in air while an increasing trend with grating

immersed in liquid.

To understand this, we first consider the diffracted field at a given distance from the aperture

$$E = E_0 + \sum_{m=1}^{\infty} E_m \exp(\frac{2\pi}{mp} x) + \sum_{m=-1}^{-\infty} E_m \exp(\frac{2\pi}{mp} x) \quad (27)$$

Here p is the pitch width. With normal incidence, we have $E_m = E_{-m}$, so Eq. (27) can be rewritten as

$$E = E_0 + \sum_{m=1}^{\infty} 2E_m \cos(\frac{2\pi}{mp} x) \quad (28)$$

Then after calculating $ILS = \left.\frac{\partial \ln(E^2)}{\partial x}\right|_{x=p/2}$, we can find $ILS \propto 1/p$ when p is large compared to the width of the aperture. This explains the decreasing trend of the DOF in air case. While for liquid immersion, as discussed before, the added high order diffracted component is the dominant factor to determine ILS. With the increase of pitch, the ratio of a/p becomes smaller, this make more energy to be distributed in high order component, so in this case the DOF is increasing.

(3) Exception

There is one exception when pitch is 600nm. At this time for TE polarization, the DOF of the grating immersed in liquid is much worse than the grating suspended in air. Figure 21 shows the ILS in this case. Although ILS with liquid immersion is better than air case for the first 90nm, it drops below threshold faster than air case, which makes the

DOF worse. This is because when pitch reaches 600nm, one new diffraction order enters for liquid immersion, which actually reduces ILS. This means all the diffracted components are not beneficial.

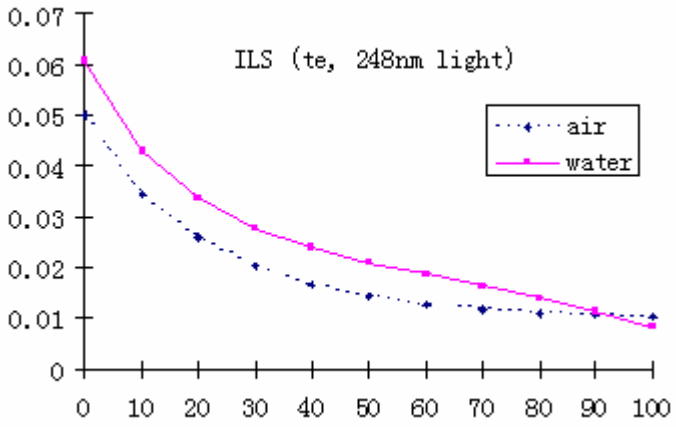

Fig. 21. ILS vs. distance from the exit plane of the grating for 600nm pitch grating with illumination of TE polarized light.

D. Conclusion

This chapter proposes a novel contact lithography technique that immerses the mask and the wafer in a non-absorbing liquid so as to improve depth-of-field. Simulation results for the diffracted near field of a chromium mask for two cases, suspended in air and immersed in liquid, show that the effect of liquid immersion will not change the DOF much for gratings with small pitch. While for large grating pitch, it significantly improves the DOF, extending DOF to more than 100nm after the pitch exceeds 1um, which is much better than conventional near-field printing. The improvement is believed to be due to the more transmitted diffracted high order components after liquid

immersion. Such high improvement of DOF will rid the need for ultrathin photoresist when printing sub-100 nm patterns, and is believed to be helpful in scanning near field optical microscopy (SNOM).

CHAPTER IV

RIGOROUS ELECTROMAGNETIC ANALYSIS OF MASK ROUGHNESS EFFECTS IN VERY HIGH NA LITHOGRAPHY

In this chapter, the effect of the mask roughness in very high NA, 193nm ArF lithography, is investigated via a rigorous electromagnetic method. Simulations of alternating phase shift mask (AltPSM) and attenuated phase shift mask (AttPSM) with one-dimensional roughness and contact mask with two-dimensional roughness are performed and the results are analyzed.

A. Overview of Major Types of Masks

Currently photomasks can be divided into two categories: binary mask and phase-shift mask (PSM). Phase-shift mask technology, which has been developed in recent years to extend the limits of optical lithography, includes attenuated, with the extreme example being chromeless phase lithography (CPL), and alternating.

1. Binary mask

A binary photomask is composed of quartz and chrome features. Light passes through the clear quartz areas and is blocked by the opaque chrome areas. Where the light hits the wafer, the photoresist is exposed, and those areas are later removed in the

develop process, leaving the unexposed areas as features on the wafer.

As feature sizes and pitches shrink, the resolution of the projection optics begins to limit the quality of the resist image. There is significant intensity even below the opaque chrome areas, due to the very close proximity of the neighboring clear quartz areas. This "unwanted" intensity affects the quality of the resist profiles, which are ideally vertical. Therefore phase-shift techniques are designed to "sharpen" the intensity profile, and thus the resist profile, which allows smaller features to be printed.

2. Attenuated phase-shift mask (AttPSM)

Attenuated phase shift masks (AttPSM) form their patterns through adjacent areas of quartz and, for example, molybdenum silicide (MoSi). Unlike chrome, MoSi allows a small percentage of the light to pass through (typically 6% or 18%). However, the thickness of the MoSi is chosen so that the light that does pass through is 180° out of phase with the light that passes through the neighboring clear quartz areas. The light that passes through the MoSi areas is too weak to expose the resist, however the phase delta serves to "push" the intensity down to be "darker" than similar features in chrome. The result is a sharper intensity profile which allows smaller features to be printed on the wafer. Figure 22 shows an attenuated phase-shift mask and the intensity in resist after it. The faint aerial image formed by the attenuated features is 180° out of phase and thus "darker" than similar chrome features formed by the binary mask.

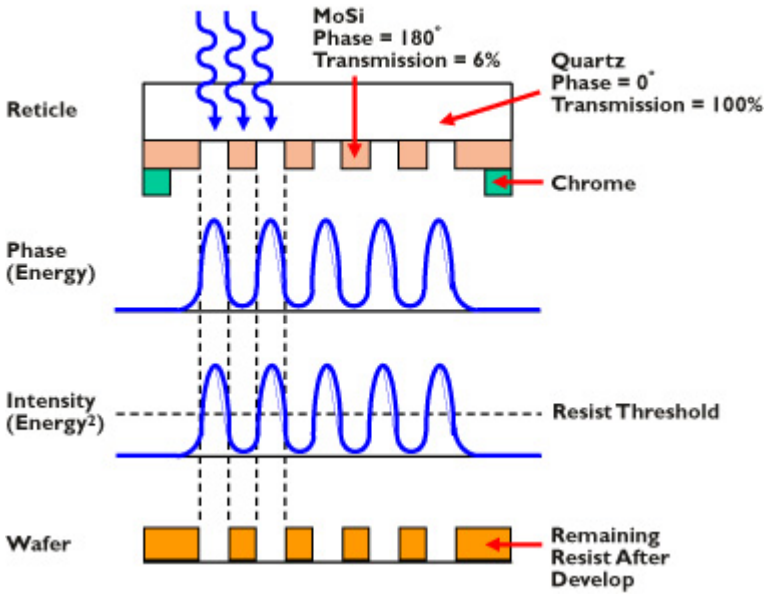

Fig. 22. Light intensity in resist after an attenuated phase-shift mask.

3. Chromeless phase lithography technology mask

Chromeless phase lithography masks can be thought of as 100% transmission attenuated phase-shift masks.[31] Features are formed on the wafer by the diffraction edges between neighboring quartz regions on the reticle that are 180 degrees out of phase. Figure 23 shows the light intensity after a chromeless phase lithography mask.

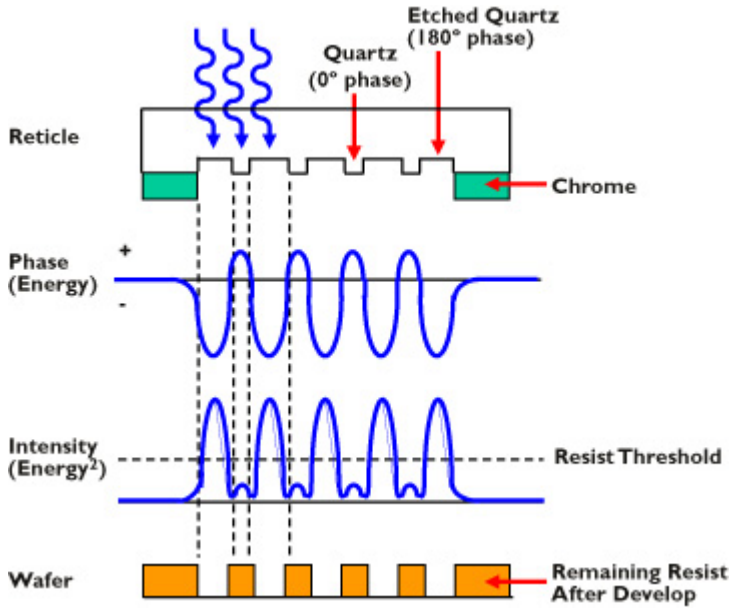

Fig. 23. Light intensity in resist after a chromeless phase lithography mask.

4. Alternating phase-shift mask (AltPSM)

Alternating phase-shift mask employ alternating areas of chrome and 180 degree shifted quartz to form features on the wafer. Alternating phase-shift mask is a powerful complex technology.[32] The process of manufacturing the mask is considerably more demanding and expensive than that for binary mask. Furthermore, the alternating phase-shift mask must be accompanied by a second "trim" mask, resulting in extra cost and decreased stepper throughput.

A typical alternating phase-shift mask and the intensity in resist after it is shown in Fig. 24. Chrome lines on the reticle are bordered on one side by quartz of phase 0°, and on the other side by quartz of phase 180°. As the phase goes from positive to negative, it

passes through 0. The intensity also goes through 0, making a very dark and sharp line on the wafer.

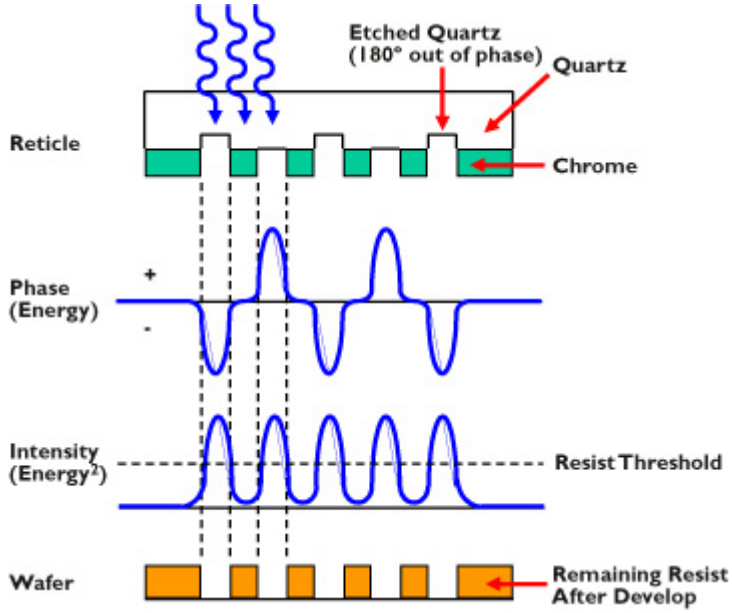

Fig. 24. Light intensity in resist after an alternating phase-shift mask

B. Introduction

In this research, we analyze the impacts of mask roughness on the printed line-edge roughness (LER) and contact holes by using rigorous electromagnetic simulation. Critical dimension (CD) error budget has become of increasing concern with the shrinkage of the printed features. One potentially significant contributor to random CD error is the mask roughness, whose effects are particularly exaggerated by flare and large Mask Error Enhancement Factor (MEEF) in sub-65nm lithography. Various models have

been developed to analyze the mask roughness effects on CD control, whereas none of them take into account the polarization effects under today's extremely high NA condition. Furthermore, the effects on 2D patterns, such as contact, are not fully analyzed, although 2D features are more sensitive to imaging errors.

C. Simulation Methods and Models

In this research, we used TEMPEST, a computer program developed by UC Berkeley that solves Maxwell's equations using a time-domain finite-difference (TDFD) algorithm, to calculate the electromagnetic field immediately after the mask and then simulate the projected wafer image with SPLAT, which calculates two-dimensional projection-printing with partial coherence based on the Hopkins' theory of partially coherent imaging.

Our goal is to investigate the effect of mask roughness on the projected aerial image in the resist. An overview of the calculation is given in Fig. 25. To generate the mask roughness, some cells in the simulation domain are assigned refractive indexes that are different from an ideal mask. This assignment is done by random number generation according to a given power spectral density (PSD) function of the mask roughness, which is assumed to be a Gaussian distribution. Figure 26 compares the light intensity distribution at the exit plane of two masks, one is an ideal mask and the other one is a mask with LER in the lateral direction, under 193nm wavelength TE illumination.

Apparently, the mask roughness results in LER and image distortion in light intensity distribution.

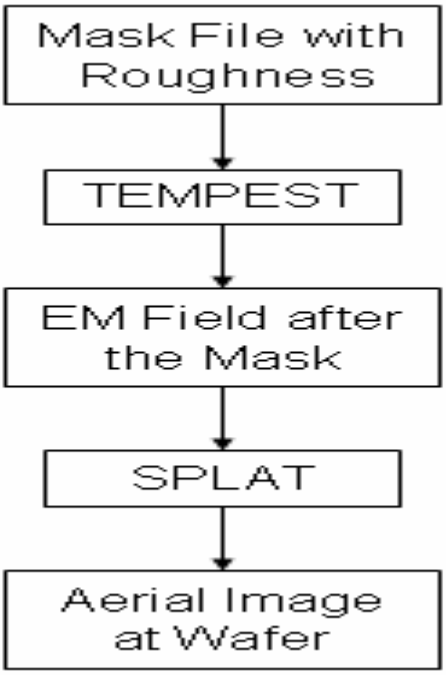

Fig. 25. Overview of the aerial image simulation flow.

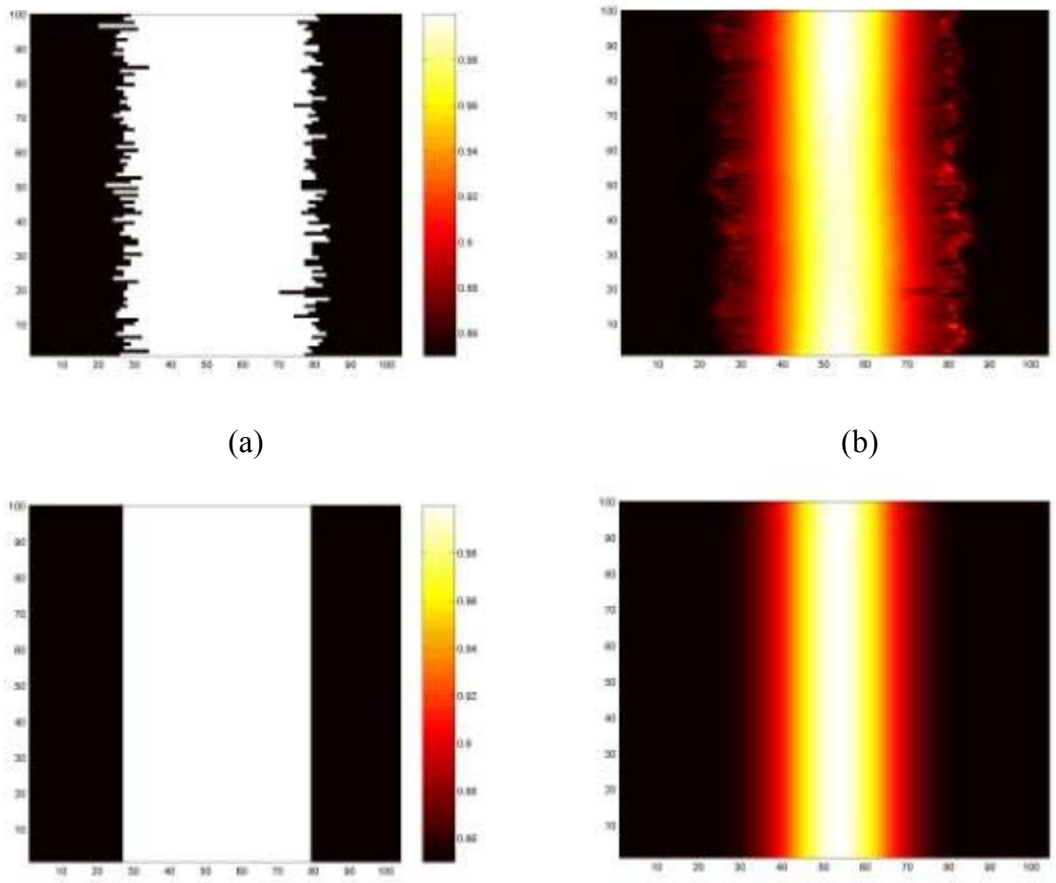

(a) (b)

(c) (d)

Fig. 26. Masks with and without roughness and their corresponding light intensity distribution immediately after the masks under 193nm wavelength TE illumination. The plots are: (a) and (b), mask with roughness and its corresponding field intensity, (c) and (d), mask without roughness.

D. Results and Discussions

1. Grating

(1) Attenuated phase-shift mask

Figure 27 shows the image light intensity distribution after the lens with a reduction factor of 4 for two equal line/space, 520nm pitch grating attenuated PSMs with 15%

transmission in the dark region. Here for the lens system, NA = 0.9 and σ = 0.9. The masks are illuminated by 193nm wavelength light with normal incidence and TE polarization from the glass side. The LER on the masks are 15nm and 30nm respectively.

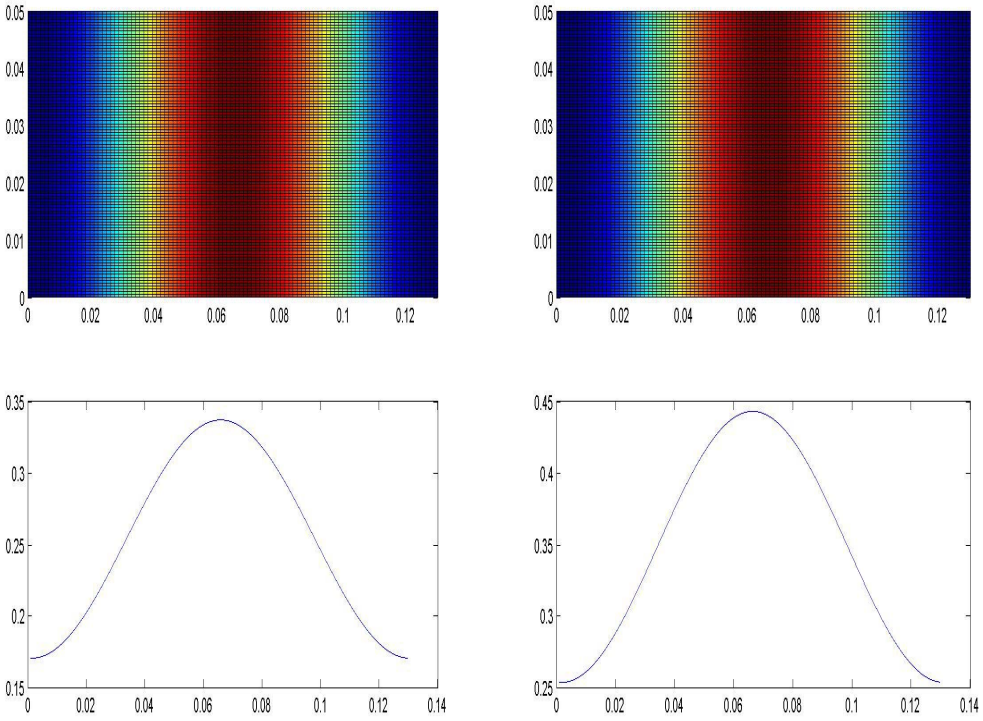

(a) (b)

Fig. 27. Image light intensity distribution and cross-section after ×4 lens for two 1:1, 520nm pitch grating attenuated PSMs with 15% transmission in the dark region, illuminated by 193nm wavelength and TE polarization. (a) 15nm LER on the mask and (b) 30nm LER on the mask.

The image LER is almost invisible for both masks, while there a considerable amount of light intensity increase for background light is observed with the increase of

LER on the mask. To understand why almost no mask roughness is transferred to the image, we can look at this problem in the frequency domain. A mask with certain LER can be modeled as the summation of the frequency components of an ideal mask and the frequency components introduced by LER. Since most of the frequency components caused by LER on the mask are in high frequency domain, they will be attenuated or blocked by the low-pass filter lens system. Therefore, the impact of mask LER on the roughness of the image light intensity is negligible. The increase of the background will be explained later in the discussion for the change of image contrast.

To further investigate the effect of LER on the mask to the contrast of the image light intensity, and the effect of illumination polarization, Fig. 28 plots the image contrast versus the LER on mask. The image contrast is decreasing with the increase of LER on the mask, for TE illumination. This increase trend of light intensity can be explained by decomposing the electrical field immediately after the mask into two parts, S(x, y) and N(x, y). Here S(x, y) denotes the electrical field under an ideal binary mask and N(x, y) denotes the electrical field variation caused by the mask roughness. So average electrical field intensity immediately after the mask is given by Eq. (29)

$$E_a = E([S(x,y) + N(x,y)]^2) = S^2 + N^2, \tag{29}$$

where S and N are power of the signal (ideal mask) and noise (mask roughness) respectively. From this equation, we can see that with the increase of mask roughness (LER of the mask), the power of the noise will increase, and so does the average

electrical field. So we can observe an increase trend of background light intensity with the increase of LER of the mask. But the high order components do not increase at the same level because of the low pass filter lens system. This causes the contrast of the image to decrease. For TM illumination, the contrast only slightly decreases. This is because the roughness is mostly in the y direction, the same as the electrical field of TE mode illumination. The TE illumination will “experience” the roughness more intensely. Therefore, the effect of mask roughness on TE mode is more significant than that on TM illumination.

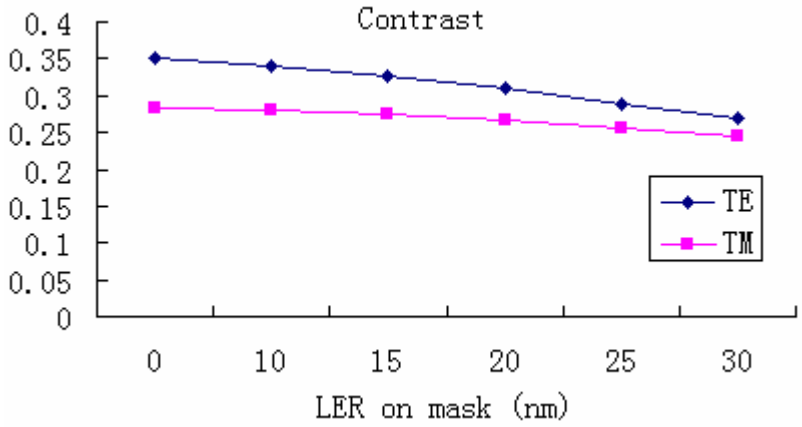

Fig. 28. Image contrast vs. LER on the mask under TE and TM polarized illumination for attPSM.

(2) Alternating phase-shift mask

The image light intensity after 4X lens for a 1:1 520nm pitch alternating PSM is shown in Fig. 29. For the lens system, NA and partial coherence are both 0.9 too. The

mask is illuminated by 193nm wavelength light with normal incidence and TE polarization for the glass side. The LER on the mask is 15nm. The same as the attPSM, the mask LER has almost no effect on the LER of the image.

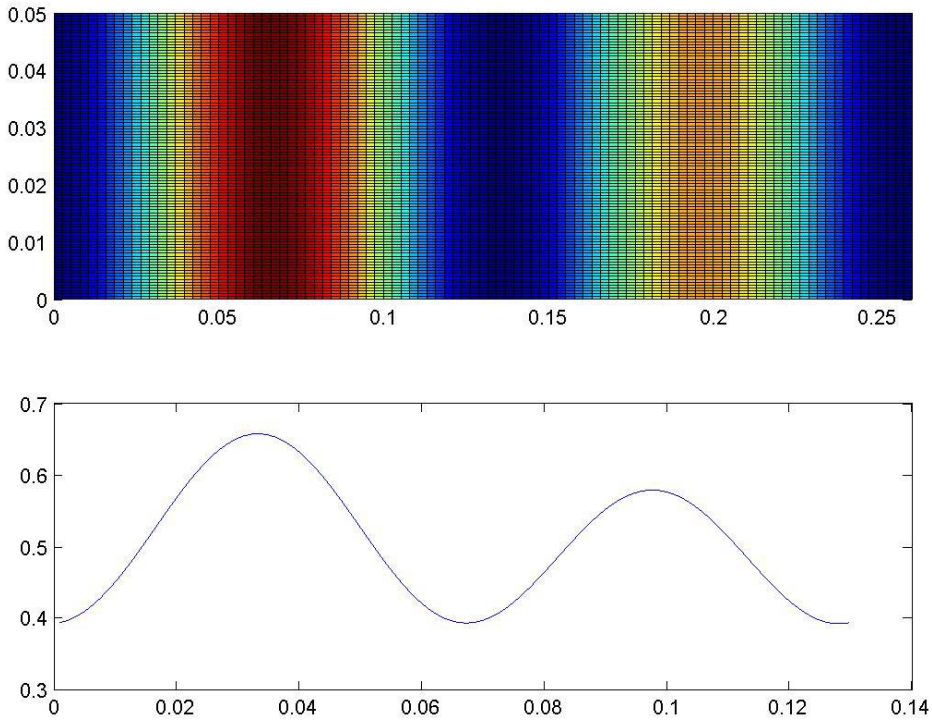

Fig. 29. The image light intensity distribution and cross-section after ×4 lens for a 1:1, 520nm pitch alternating PSM.

Figure 30 plots the contrast versus the LER on mask for both TE and TM illuminations. In contrast to the attPSM, the LER on the mask does not have much effect on the image background intensity and contrast.

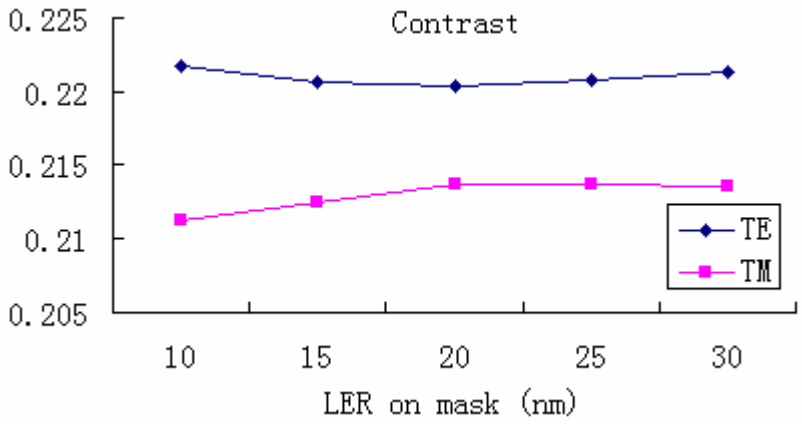

Fig. 30. Image contrast vs. LER on the mask under TE and TM polarized illumination for altPSM.

2. Contact

(1) Attenuated phase-shift mask

Our simulation shows that the attenuated PSM is incapable to print 65nm contact by directly making a 260nm by 260nm square in the mask. The light intensity at the center of the contact is lower than the outside after the projection of the 4X lens. This is due to the intense 2-D waveguide effect caused by the small contact features. The phase difference between the bright region and the dark region in the mask is no longer 180°. Figure 31 plots the light phase distribution immediately after the mask. The phase difference between the bright region and the dark region is almost within 90°.

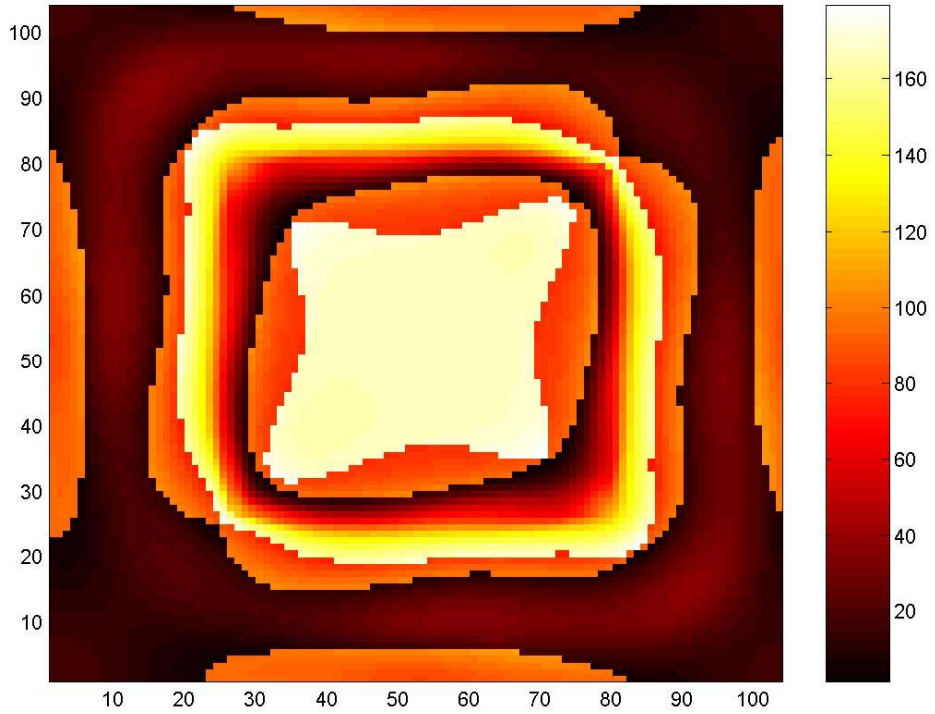

Fig. 31. Phase distribution of the light field immediately after the attenuated PSM for a contact under illumination of a circular polarized incident field.

(2) Cr binary mask

The traditional Cr binary mask achieves relatively better performance than attenuated PSM in printing contact, although the contrast of the projected image is low, around 0.15. As expected, the LER of the image is very small, but still there is certain variation of the contact average diameter caused by LER on the mask. Figure 32 plots the average diameter of the contact versus LER on the mask. Unlike the result of grating mask, the image background intensity first increases with the LER on the mask, then drops (the same trend as the average diameter since the threshold intensity is the same).

As explained before, the increase of the image background intensity is due to the power of the mask noise (LER on the mask). With the increase of LER on the mask, the scattering of the incident wave will also increase significantly, which causes the light intensity to drop. The scattering at the surface of the contact mask is much significant than that at the surface of the grating mask. Therefore, although the light intensity after a grating mask increases due to LER on the mask, the light intensity after a contact mask decreases.

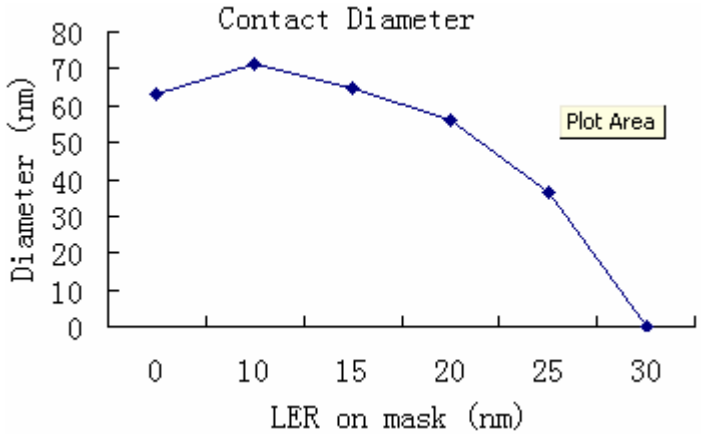

Fig. 32. Average contact diameter vs. LER on the mask for Cr mask.

E. Conclusion

This chapter investigates the effect of the mask roughness in very high NA, 193nm wavelength lithography. Simulation results for grating mask show that mask roughness will not be transferred to the projected light image. Due to the low-pass filter lens system, the high frequency components of the roughness are attenuated. The image background

intensity is increased with the increase of mask roughness, which is due to the increase power of the mask noise (LER on the mask). Simulation for contact shows that attenuated PSM is not capable to print 65nm contact due to the waveguide effect which changes the phase difference between the dark region and the bright region significantly. While for the traditional Cr mask, it shows some promise in printing 65nm contact. The effect of mask roughness in printing contact is similar to that in printing grating, except that with high mask roughness, the image background intensity will decrease due to the increased scattering at the surface of the contact mask.

CHAPTER V

CONCLUSION

Both resist metrology techniques and optical modeling methods are investigated for deep-UV lithography.

Chapter II presents a novel methodology of simultaneously measuring the non-Fickean acid diffusivity and deprotection rate in positive CAR by monitoring impedance change during PEB. A comprehensive PEB model is proposed that includes deprotection reaction, free volume generation, resist shrinkage and acid diffusion. The experiment was done with Shipley UV5 resist and all the model parameters are extracted from RC curves by using divide-and-conquer strategy. In particular, deprotection rate constant, dependence factor of diffusivity on deprotection level and diffusivity are calculated from log slope of RC curves, so they are free of measurement errors other than RC. Therefore this methodology is supposed to be very accurate.

It is found that free volume escapes to air or is absorbed by polymer at a very rapid rate, indicating that free volume enhancement of acid diffusion or reaction is negligible. The extracted diffusivity agrees with the previous work considerably well. The simulated RC curves fit experimental data very well with an RMS error less than 0.1%, indicating high accuracy of our methodology.

Chapter III proposes a novel contact lithography technique that immerses the mask

and the wafer in a non-absorbing liquid so as to improve depth-of-field. Simulation results show that the effect of liquid immersion will not change the DOF much for gratings with small pitch. While for large grating pitch, it significantly improves the DOF, extending DOF to more than 100nm after the pitch exceeds 1um. The improvement is believed to be due to the more transmitted diffracted high order components after liquid immersion. Such high improvement of DOF will rid the need for ultrathin photoresist when printing sub-100 nm patterns, and is believed to be helpful in scanning near field optical microscopy (SNOM).

Chapter IV investigates the effect of the mask roughness in very high NA, 193nm wavelength lithography. Simulation results for grating mask show that mask roughness will not be transferred to the projected light image. Due to the low-pass filter lens system, the high frequency components of the roughness are attenuated. The image background intensity is increased with the increase of mask roughness, which is due to the increase power of the mask noise (LER on the mask). Simulation for contact shows that attenuated PSM is not capable to print 65nm contact due to the waveguide effect which changes the phase difference between the dark region and the bright region significantly. While for the traditional Cr mask, it shows some promise in printing 65nm contact. The effect of mask roughness in printing contact is similar to that in printing grating, except that with high mask roughness, the image background intensity will decrease due to the increased scattering at the surface of the contact mask.

REFERENCES

[1] P. J. Silverman, Intel Technol. J. **6**, 55-61 (2002).

[2] W. D. Hinsberg, F. A. Houle, M. I. Sanchez, and G. M. Wallraff, IBM J. Res. & Dev. **45**, 667-682 (2001).

[3] G. Wallraff, J. Hutchinson, W. Hinsberg, F. Houle, P. Seidel, R. Johnson, and W. Oldham, J. Vac. Sci. Technol. B **12**, 3857-3862 (1994).

[4] L. Schlegel, T. Ueno, N. Hayashi, and T. Iwayanagi, J. Vac. Sci. Technol. B **9**, 278-289 (1991).

[5] M. Zuniga and A. R. Neureuther, J. Vac. Sci. Technol. B **13**, 2957-2962 (1995).

[6] S. Postnikov , M. Stewart, H. Tran, M. Nierode, D. R. Medeiros, T. Cao, J. Byers, S. Webber, and C. G. Wilson, J. Vac. Sci. Technol. B **17**, 3335-3338 (1999).

[7] A. A. Krasnoperova, M. Khan, S. Rhyner, J. W. Taylor, Y. Zhu, and F. Cerrina, J. Vac. Sci. Technol. B **12**, 3900-3904 (1994).

[8] J. L. P. Jessop, S. N. Goldie, A. B. Scranton, and G. J. Blanchard, J. Vac. Sci. Technol. B **20**, 219-225 (2002).

[9] J. Nakamura, H. Ban, K. Deguchi, and A. Tanaka, Jpn. J. Appl. Phys. **30**, 2619-2625 (1991).

[10] T. H. Fedynyshyn, J. W. Thackeray, J. H. Georger, and M. D. Denison, J. Vac. Sci. Technol. B **12**, 3888-3894 (1994).

[11] T. Itani, H. Yoshino, S. Hashimoto, M. Yamana, N. Samoto, and K. Kasama, J. Vac. Sci. Technol. B **14**, 4226-4228 (1996).

[12] F. A. Houle, W. D. Hinsberg, M. Morrison, M. I. Sanchez, G. Wallraff, C. Larson, and J. Hoffnagle, J. Vac. Sci. Technol. B **18**, 1874-1885 (2000).

[13] Edited by E. Reichmanis, C. W. Frank, and J. H. O'Donnell, *Irradiation of Polymeric Materials: Processes, Mechanisms, and Applications* (American Chemical Society, Washington DC, 1993).

[14] M. Cheng, L. Yuan, E. Croffie, and A. R. Neureuther, J. Vac. Sci. Technol. B **20**, 734-740 (2002).

[15] E. Croffie, M. Cheng, and A. R. Neureuther, J. Vac. Sci. Technol. B **17**, 3339-3344 (1999).

[16] N. Jakatdar, J. Bao, C. J. Spanos, R. Subramanian, and B. Rangarajan, Proc. SPIE, **3678**, 275-282 (1999).

[17] E. Betzig, J. K. Trautman, T. D. Harris, J. S. Weiner and R. L. Kostelak, Science **251**, 1468-1470 (1991).

[18] T. A. Savas, M. L. Schattenburgh, J. M Carter, and H. I. Smith, J. Vac. Sci. Technol. B **14**, 4167-4170 (1996).

[19] H. H. Solak, D. He, W. Li, and F. Cerrina, J. Vac. Sci. Technol. B **17,** 3052-3057 (1999).

[20] J. A. Rogers, K. E. Paul, R. J. Jackman, and G. M. Whitesides, J. Vac. Sci. Technol. B **16**, 59-68 (1998).

[21] Hai Dang, Jackie Lim-Piu Tan, and Mark W. Horn, J. Vac. Sci. Technol. B **21**, 1143-1148 (2003).

[22] H. Schmid, H. Beibuyck, B. Michel, O. J. F. Martin and N. B. Piller, J. Vac. Sci. Technol. B, **16**, 3422-3425 (1998).

[23] M. Colburn, S. Johnson, M. Stewart, S. Damle, T. Bailey, B. Choi, M. Wedlake, T. Michaelson, S. V. Srenivasan, J. Ekerdt, and C. G. Willson, Proc. SPIE, **3676**, 379-389 (1999).

[24] B. Lin, Microelectron. Eng. **6**, 31-51 (1987).

[25] A. Wong and T. Pistor, *TEMPEST version 6.0*, ERL, UC Berkeley, 2000.

[26] Edited by E. D. Palik, *Handbook of Optical Constants of Solids* (Academic Press, San Diego, 1998).

[27] S. J. McNcb and R. J. Blaikie, Appl. Opt., **39**, 20-25 (2000).

[28] H. A. Bethe, Phys. Rev., **66**, 163-182 (1944).

[29] U. Schröter and D. Heitmann, Phys. Rev. B, **58**, 15419-15421, (1998).

[30] S. J. McNab, R. J. Blaikie, and M. M. Alkaisi, J. Vac. Sci. Technol. B, **18,** 2900-2904 (2000).

[31] M. M. Alkaisi, R. J. Blaikie, and S. J. McNab, J. Vac. Sci. Technol. B, **16,** 3929-3933 (1998).

[32] A. K. Wong and A. R. Neureuther, IEEE Trans. Electron Devices **41**, 895-902 (1994).

VITA

Chao Liu was born in Wuhan, Hubei Province, People's Republic of China. He received a B.S. in electronic engineering from Tsinghua University (P. R. China) in July 2002. Upon graduation, he began attending Texas A&M University in August 2002 and received his M.S. degree in electrical engineering in August, 2005. He can be reached at the following address:

Department of Electrical Engineering

Texas A&M University, College Station, TX, 77843-3128